Title: CA1 Engram Cell Dynamics Before and After Learning

Authors: Amy Monasterio[1], Caitlin Lienkaemper[2,4], Siria Coello[3], Gabriel K. Ocker[2,4], Steve Ramirez[2,3,5,6] and Benjamin B. Scott[2,3,5,6]

[1]Graduate Program for Neuroscience,
[2]Center for Systems Neuroscience,
[3]Department of Psychological and Brain Sciences,
[4]Department of Mathematics and Statistics,
[5]Center for Neurophotonics, Boston University, Boston, MA, USA
[6]Equal Contribution

Highlights

- Tracked calcium activity and Fos tagging in CA1 across time and learning.
- Spontaneous activity days before learning predicts TetTagging.
- No observed changes in TetTagged cell correlations in spontaneous activity after learning.
- Modeling suggests E/I balance regulates engram dynamics.

Keywords

Hippocampus, engram, learning, immediate-early gene, spontaneous activity, memory

Correspondence: bbs@bu.edu and dvsteve@bu.edu

Summary

A fundamental question in neuroscience is how memory formation shapes brain activity at the level of populations of neurons. Recent studies of hippocampal 'engram' cells, identified by immediate-early genes (IEGs) induced by learning, propose that these populations act as a neuronal substrate for memory storage. The current framework for engram formation proposes that cells join ensembles based on increased intrinsic excitability, and that after initial learning, they co-activate to support memory retrieval. However, direct evidence of how engram population dynamics evolve across learning is limited. Here we combined activity-dependent genetic tagging and two-photon calcium imaging to characterize CA1 engram population activity before and after learning. We observed that spontaneous activity two days before learning predicted genetic tagging, consistent with a model in which spontaneous fluctuations bias cells into forming engram assemblies. Surprisingly, we were unable to detect increased spontaneous activity rates or pairwise correlations amongst tagged CA1 neurons after learning. These results were consistent with computational network models that incorporate strong and specific inhibitory connections, supporting the idea that excitatory/inhibitory balance in CA1 may play a key role in engram dynamics. Together these results highlight a potential role for slow time scale excitability fluctuations in driving engram formation and suggest that excitatory-inhibitory balance may regulate engram cell co-activation.

Introduction

While decades of research have established the central role of the hippocampus in episodic memory formation, the precise mechanisms by which neuronal populations are selected to participate in individual memories are still undefined. A rich body of literature suggests that learning drives plasticity within populations of neurons activated by experience.[1,24/16/24 12:36:00 PM] This plasticity involves a dynamic series of changes in gene expression and synaptic connectivity which are thought to drive corresponding changes in activity patterns at the population level. Together these changes in gene expression, connectivity, and activity are thought to constitute a neurophysiological memory trace and are often referred to as a memory engram.[2]

Historically, two complementary approaches have been used to characterize such engrams. First, in vivo population recording of cells active during memory tasks and spatial navigation has been fundamental in understanding the coding properties of hippocampal neurons.[34/16/24 12:36:00 PM] Second, so-called 'engram-tagging' studies in the past decade have used IEG expression, such as Fos or Arc, to identify populations of neurons and to demonstrate their necessity and sufficiency in driving the behavioral expression of memory.[4–64/16/24 12:36:00 PM] While numerous cases of artificial manipulation of engram-tagged populations have driven a suite of behaviors ranging from fear recall (i.e., freezing[5,6]), approach,[7,8] and motivated behaviors,[9,10] surprisingly less is known about how patterns of activity in engram assemblies change with learning.

Understanding the causal thread between cellular activity, memory, and behavior will require linking short timescale mechanisms (e.g., gene expression, changes in spontaneous activity) with longer time scale readouts (e.g., post-learning population activity, behavioral

phenotypes). To date, a handful of studies have performed functional recordings of hippocampal engram-tagged cells during spatial navigation after Fos-tagging. Engram cells (i.e. Fos-positive cells) demonstrated distinct spatial selectivity and population dynamics from non-engram (i.e. Fos-negative) cells, which are thought to support contextual representations comprising memory.[11,12] Despite this, the change in engram cell activity across memory formation has not been described.

There are two complementary hypotheses relating activity dynamics to engram formation. First, a growing body of work has investigated how pre-existing cellular excitability influences the recruitment of cells during novel experiences.[13,144/16/24 12:36:00 PM] These studies propose that intrinsic fluctuations in cellular excitability levels *before* learning dictate which cells become part of a memory engram, commonly referred to as the allocation hypothesis. Second, IEG-based engram-tagging studies have proposed that coactivity among engram cells emerges *after* learning and therefore comprises a physiological correlate for memory.[15–17] This hypothesis is supported by recent work identifying structural and synaptic properties of engram cells in vitro–namely, that engram cells show a higher level of connectivity between each other compared to non-engram cells.[17–194/16/24 12:36:00 PM]

To evaluate these hypotheses, we used a combination of activity-dependent genetic tagging, longitudinal calcium imaging, and computational modeling to characterize spontaneous activity in CA1 engram populations before and after learning. First, we discovered that spontaneous activity during periods of rest before learning was informative for engram allocation at a time point up to two days before immediate-early gene expression. Surprisingly, after learning we did not observe changes in engram cell activity rate or correlations in vivo. These data were best described by neural network models with strong inhibitory control, suggesting a key role for inhibitory/excitatory (E/I) balance in regulating engram cell dynamics. Overall, we view our findings as an important stepping stone to bridge the gap in knowledge regarding the underlying physiology of memory-engram populations across learning.

Results

In vivo tracking of calcium dynamics of engram and non-engram cells over days

In order to record engram dynamics over time, we first evaluated the feasibility of tracking engram and non-engram cells and their corresponding population activity by using two-color two-photon imaging in CA1 across days. We did this by combining the commonly used TetTag system to identify engram cells with transgenic Thy1-GCaMP6f mice to record population calcium activity (Figure 1A). During recording sessions, head-fixed mice could walk on a rotating disk and we measured locomotion state. We used a kinematic mounting device[20] to register the head across imaging sessions and fields of view were manually aligned. Using this system, we could reliably record calcium activity (GCaMP) and tet-driven mCherry in the same populations days apart (Figure 1B). Across sessions, we performed cell registration with previously published approaches (i.e., CellReg[21]) followed by manual evaluation of registered pairs (Supplementary Figure 2A-B, Methods). In a 405 by 405 micron field of view we observed an average of 193 +/-

6 spontaneously active neurons. We were able to track the same cells across days (Supplementary Figure 2A) and observed a turnover in the pool of active cells registered across 4 days (Figure 1C). 55.7% +/- 2% of cells from Day 0 remained active on Day 4, while 44.3% +/- 2% percent of cells turned over from Day 0 to Day 4. Tet-driven mCherry expression was used to identify putative engram cells (Supplementary Figure 1, Methods). These data indicate the feasibility of tracking activity patterns in engram and non-engram neurons across multiple days.

Recording CA1 population dynamics before and after learning

To assess how the activity of engram cells changes over time, we recorded CA1 populations before and after learning. Day 0 baseline spontaneous activity was recorded in a population of CA1 pyramidal neurons prior to Fos-tagging (Figure 1A). On Day 2 mice either underwent a 3-shock contextual fear conditioning protocol (FC, n=5, Supplementary Figure 1F) or remained in the homecage (HC, n=7) as a neutral experience, to drive Fos-tagging with mCherry in dorsal CA1. Dox was replaced after tagging to close the window for mCherry labeling, and a second recording of spontaneous activity took place on Day 4 (Figure 1A-B). We classified cells as either engram or non-engram based on their Day 4 mCherry expression (Figure 1D-E, see Methods). Approximately ~30% of registered cells across both days were mCherry+ and therefore classified as engram cells (Figure 1G). However, there was an increase in the proportion of newly recruited cells in the FC group compared to HC (Figure 1F), suggesting that learning may contribute to a shift in the pool of spontaneously active engram cells across different contexts and time.

Increased activity prior to tagging biases TetTag labeling

With this approach, we first sought to test the first prediction of the allocation hypothesis, namely if spontaneous activity before learning could predict engram tagging. To do this, we deconvolved calcium activity and calculated event rates for each cell on Day 0 such that event rates were weighted by the size of transients (Methods). We separated cells into deciles within each animal, from least to most active (Figure 2A-B). Cells in different deciles were distributed in space throughout the FOV (Figure 2D). Overall, engram cells with higher spontaneous activity were more biased to be engram cells (Figure 2C). We observed a significant positive correlation between a cell's decile and the likelihood it would be Fos-tagged (Figure 2E). Interestingly, this effect was seen in both FC and HC groups (Supplementary Figure 3). Spontaneous activity during rest, but not during locomotion, was correlated with engram tagging (Figure 2F, Supplementary Figure 3). These results suggest that increased activity at a time point up to 48 hours before Fos-tagging correlates with allocation, independent of which experience was tagged (aversive footshock or neutral homecage).

Engram cells do not increase activity after learning, but maintain higher rates compared to non-engram cells

We next asked if engram cells maintained higher spontaneous activity across days, and if their spontaneous activity changed after fear learning. To address this, we identified active cells across both Day 0 and Day 4 and compared their mean calcium event rate across each session. Interestingly, engram cells had higher activity rates at both timepoints in both FC and HC mice

(Figure 3C), in agreement with previous recordings of engram cell activity in CA1.[11,12] On average, we saw no increase in activity amongst engram cells from Day 0 to Day 4 in either group of mice (Figure 3A). To control for variability in locomotion behavior (Supplementary Figure 4A) and the effects of locomotion on activity levels (Supplementary Figure 4B-C), we removed periods of locomotion and focused only on periods of quiet rest. Again, there was no change in rate among either engram or non-engram populations across mice (Supplementary Figure 4D-E). Overall, our results suggest that Fos-identified engram populations display higher levels of spontaneous activity, that was not dependent on learning, at time periods ranging from two days before to two days after IEG-tagging.

Correlations between engram cells are unchanged after learning

A key prediction of many engram-tagging studies is that after learning, engram neurons have stronger synaptic connectivity that drives their correlated activity. To test this prediction, we compared the correlations of engram cell activity on Day 0 and Day 4. All mean correlations were significantly greater than a shuffled control (Supplementary Figure 5A-B). Surprisingly, we observed no significant increases in mean correlation of engram cells from Day 0 to Day 4 in either FC or HC groups (Figure 4B). To account for potential time lags between pairs of cells, we repeated these correlations across a range of time bins in our deconvolved traces. We saw no increase in correlations between engram cells across timescales ranging from 0.13 seconds to 4 seconds (Supplementary Figure 5C-D). Overall, we observed no significant increases in correlations from D0 to D4 across this range of bin sizes (Supplementary Figure 5C-D). Finally, to evaluate the possibility of 'washing-out' a small subset of highly correlated cells, we evaluated if the distribution of the most highly correlated cells changed across days between engram or non-engram populations (Supplementary Figure 5E-F). Specifically, we examined the distribution of highly correlated cells across D0 to D4 and found that a similar amount of highly correlated cell partners in both populations (Supplementary Figure 5E-F). These data suggest that under conditions of spontaneous activity, consistent learning-related increases in correlations between TetTagged cells were minimal or absent.

Computational model of CA3-CA1 engram dynamics

Previous studies have demonstrated evidence of increased synaptic connectivity between CA3 engram cells and CA1 engram cells.[17,19] Therefore, we were surprised not to detect increased activity or correlations between engram cells after learning. To explore potential mechanisms for this observation, we implemented a spiking neural network model of CA3 and CA1 (Figure 5A; see Methods).[22] We embedded a population of engram neurons in CA3 and CA1 by increasing synaptic weights amongst a subpopulation of neurons (described by parameter *h* in the model, Figure 5A). In this baseline model, we observed increased firing rates and correlations between engram cells (Figure 5B-C, Supplementary Figure 6A). Since we did not observe these changes in vivo, we wondered what circuit mechanisms could be present in CA1 and CA3 that might reduce or cancel these effects. We considered three potential mechanisms: 1) engram-specific homeostatic inhibition, 2) strong global inhibition, and 3) noisy tagging.

Homeostatic inhibition maintains firing rates, while global inhibition maintains network correlations

First, we considered a homeostatic inhibition mechanism in which inhibitory inputs onto engram cells increase to maintain engram cells' firing rates.[23] In this version of the network, parameters h_{I1}, h_{I3} define the inhibitory input onto CA1 and CA3 engram cells respectively (Figure 5A, see Methods). The weights h_{I1} h_{I3} were chosen to maintain firing rates of engram cells, after potentiating excitatory engram weights (Figure 5C). While this approach was sufficient to prevent increases in engram cell firing, similar to our in vivo data (Figure 3A), this network still exhibited stronger correlation between engram cells than non-engram cells (Figure 5C-D).

Next, we considered how the strength of global inhibition controlled the dynamics of engram cells after learning. We parameterized the strength of global inhibition with the variable g, i.e. the strength of inhibitory to excitatory connections (Figure 5A). We varied g between 1 and 3, and potentiated engram weights with strength h=2, adjusting h_{I1}, h_{I3} to homeostatically maintain firing rates (Figure 5E). Interestingly, this model strongly reduced but did not completely eliminate increases in correlation between engram cells (Figure 5F). However, this network did produce the best qualitative fit to our in vivo data. While our model incorporates stochasticity in neuron activity, it does not explicitly model sources of noise in this process, including measurement noise. These simulations suggest that strong global inhibition is sufficient to mask increased correlations within strongly connected engram networks.

'Noisy' tagging is a potential mechanism for reduced correlations

Until now our simulations have assumed accurate identification of engram and non-engram populations. However, we wanted to consider the impact of false positives (i.e. mCherry tagging in non-engram cells) on our data. To evaluate the effect of false positives on population dynamics, we simulated a 'noisy-tagging' condition in our initial model (Figure 5A, Figure 5G-H). This model was parameterized by the parameter p_{fp} which set the probability that a non-engram cell was mis-identified as an engram cell (Figure 5G). For low values of h, this model was sufficient to suppress increases in firing changes and correlations between engram cells (Figure 5H). This suggests that with subtle changes in synaptic strength, a high degree of false tagging can wash out any increases in pairwise correlations between true engram cells.

Strong global inhibition model predictions

Our recordings and simulations have focused on spontaneous dynamics, which we modeled with weak drive onto CA3 cells. Here we considered how reactivation, modeled as strong drive onto CA3 engram cells, would alter neural dynamics in CA1. We considered reactivation within the context of the strong global inhibition model, which best fit spontaneous data (Figure 6A). Stimulation of half of the CA3 engram cells (Figure 6B), produced a dramatic change in the population activity across the network (Figure 6B). Surprisingly, reactivation resulted in decreased firing rates in CA1 non-engram cells (Figure 6C). As expected, reactivation resulted in increased correlations in CA1 and firing rates in engram cells (Figure 6C-D). Interestingly, our model predicts that correlations in CA1 are driven primarily by local inhibitory connectivity within CA1, rather than

inputs from CA3 (Supplementary Figure 6B). Together, these results provide quantitative predictions that can be tested in future experiments.

Discussion

Here we investigated the dynamics of TetTagged cells in CA1 before and after learning using an intersectional approach that combined in vivo imaging of cell populations with computational modeling. These data revealed several surprising findings. First, we observed that activity up to two days before fear conditioning was predictive of IEG-tagging state. Second, and contrary to expectation, we did not observe am increase in correlated activity between tagged cells after learning. Finally, comparison of neural data with spiking network models suggested a key role for inhibitory control of engram cell dynamics and highlight the influence of noise in TetTagging on population measures. Together, these results reveal novel aspects of TetTagged engram populations and suggest potential future directions for investigation.

Our finding that spontaneous dynamics prior to fear conditioning correlate with IEG-tagging supports the popular allocation model of engram formation.[13,14] Previous support for the allocation model came initially from manipulation studies, in which over-expression of CREB or optogenetic stimulation of cells prior to learning increased their likelihood of reactivation, during memory recall.[14,24–28] More recently, a study used in vivo imaging, in a paradigm similar to the one we describe here, to track direct endogenous fluctuations in calcium dynamics prior to IEG-tagging.[28] They found that cells with higher levels of activity several hours prior to fear conditioning were more likely to undergo IEG-tagging. Together these previous data and our results support a model in which intrinsic fluctuations in neural dynamics within the hippocampus regulate engram formation.

While there is wide support for this model of engram formation, several aspects of the allocation model have yet to be characterized. First, it remains unclear whether these intrinsic fluctuations in the hippocampus are cell autonomous, such that each cell cycles independently through periods of high and low excitability, or whether pre-existing networks fluctuate together.[24–26,28,] Furthermore, the timescales of these intrinsic fluctuations are unknown. On the one hand some authors have argued for short timescales on the order of minutes to hours [25,28,29] , whereas others have suggested that intrinsic fluctuations could exist across multiple days, as observed by linkage of fear memories across two days.[30,31] Available data, including the results presented here (e.g. Figure 2E-F, Figure 3D), are consistent with the existence of heterogenous dynamics, including both short and long timescale intrinsic fluctuations.

In this study, we demonstrate that elevated activity during quiet rest best predicts future IEG-tagging. This observation is interesting given that the hippocampus displays highly structured dynamics such as sharp-wave ripples (SWRs), replay and preplay during rest and offline periods.[32–35] This structured activity is thought to support successful encoding and consolidation of episodic experiences, and contribute to memory guided decision-making.[32,36] While we did not explicitly identify sequences of activity in our data, one interesting future direction would be to investigate whether engram cell assemblies display reliable and specific sequences of firing prior to learning and tagging, and whether these sequences change after learning.

Interestingly, in our analyses, we found the relationship between prior spontaneous activity and engram-tagging existed in both aversive (FC) or neutral (HC) conditions, which suggests that

increased spontaneous activity is predicts Fos-tagging in the absence of fear learning. In prior work, FC-tagged cells drove freezing while neutral-tagged cells did not.[5,7,8,37,38] While this approach focuses on the role of valenced experiences in mediating the ability of Fos-tagged cells to drive behaviors, it lacks the ability to compare the similarities between neutral or fear-related cell assemblies. We speculate that these "homecage cells" are nonetheless part of an ensemble unrelated to fear. Here, we decouple behavioral experience from physiology of engram cells by identifying existing similarities in Fos-tagged cells regardless of experience or valence.

Surprisingly, we were unable to detect increased correlations between engram cells after learning. We demonstrated strong global inhibition in CA3-CA1 as one potential circuit mechanism that influenced correlations amongst engram cells. Homeostatically increased inhibition onto engram cells alone maintained their firing rates but had a small effect on CA1 engram cell correlations. A role for inhibitory signaling into IEG-expressing cells has strong preliminary support from both theoretical[39–41] and in vivo studies, which have identified a role for parvalbumin-mediated inhibition onto engram cells, including their role in maintaining the size of engram populations,[42] as well as their involvement in bidirectional inhibitory plasticity onto CA1 engram neurons.[43] Additionally, we demonstrated that noise in the labeling strategy may also influence the ability to detect pairwise correlations among a small engram population. Future experiments may seek to systematically characterize differences in false-positive and false-negative rates in activity-dependent tagging strategies (see Limitations). Overall, we aimed to create a relatively simple modeling framework that will serve to ground future in vivo experiments in a tractable model for activity dynamics in the dorsal hippocampus. For example, our reactivation simulation generated predictions about downstream CA1 dynamics in engram cells. These predictions could be addressed with in vivo optogenetic or chemogenetic manipulations of engram cells in upstream DG/CA3 with simultaneous imaging.

Limitations of the study

A key issue with many IEG-tagging studies lies in the difficulty of estimating the onset and duration of the tagging window. This problem is particularly acute with the TetTagging system when doxycycline is administered in the animal's diet. We chose this system for its wide use in engram-tagging studies and the evidence that cells labeled with this system can drive memory behaviors. However, several unknowns limit the precise knowledge of onset and duration of tagging including the timing of the animal's last meal, the half-life of doxycycline (which could be variable across animals), the concentration of doxycycline needed to suppress gene expression (1 mg/kg dose minimum[44], but concentrations may be lower in the brain[45]) and the half-life of tTA-protein. Previous studies have suggested that the TetTagging window opens within 24 hours of food removal[5] however finer timescale measurements have not been performed to our knowledge. Moreover, we point out that there may be high variability animal to animal based on individual and strain differences[46] in the rate of doxycycline metabolism and the timing and amount of dox food consumed. Future studies could more precisely measure the onset and duration of Tet-tagging. Alternatively future studies could shift to more recently developed tagging systems with greater temporal precision.

Other studies have utilized the TRAP2[28,47] system as it labels a smaller proportion of CA1 during a shorter time window, around 5% of spontaneously active cells[28] which is much lower than the 30% observed with the TetTag system. Future experiments may more systematically

characterize differences between tagging techniques[48,494/16/24 12:36:00 PM] and their consequential impacts on functional readouts of engram population activity. In addition to the TRAP2 system, newly developed methods that utilize faster timescale light-dependent systems include CaL-Light[50], scFLARE[51,52] and FLiCRE[53] which permit genetic tagging of cells on a seconds-timescale. However, care should be taken when selecting methods as these more temporally restricted tools rely on light activation for tagging that may preclude simultaneous photoexcitation for functional imaging. Thus, employing more temporally restricted techniques combined with experimental designs in which behavior is monitored longitudinally, can be done systematically in future studies to reveal the mechanisms surrounding memory allocation.

Finally, our results highlight the need for future work investigating engram dynamics across different behavioral states. Here, we focused on spontaneous dynamics for two reasons. First, our initial computational model (Figure 5A), similar to prior studies, have shown that synaptic changes expected during learning result in changes in correlated activity of spontaneous firing.[22,544/16/24 12:36:00 PM] Second, activity during quiescent periods has demonstrated the existence of emergent dynamics in hippocampal activity, such as replay during memory periods of spatial tasks.[34,35] Indeed, it is possible that increased correlations between engram cells are gated by context, or behavioral state such as memory retrieval. Given evidence that IEG-tagged place cells have some level of context-specificity,[11] it is possible that we under sampled the engram population in our imaging context, and that some engram cells which remained silent in our imaging context could have informative dynamics in other environments or behavioral states. Relatedly, recent studies demonstrate engram cell reactivation optimally drives retrieval during conditions of high coherence between encoding and retrieval.[51] Future experiments may directly apply our approach here, and integrate it with head-fixed behavioral paradigms such as head-fixed aversive trace eye puff conditioning[55] or contextual tail shock conditioning in VR,[56] in order to characterize how activity during encoding or retrieval may relate to engram cell emergence or population dynamics.

Conclusion

Ultimately, we view our findings as building upon the basic mechanisms of hippocampal engram cell physiology in order to integrate what is known about hippocampal dynamics during memory with emergent studies of IEG-based engram-tagging to inform a more holistic understanding. To successfully integrate these approaches, it is crucial to combine measurements of population physiology over time with IEG-tagging techniques and measure endogenous activity. Towards that end, here we combined in vivo imaging, IEG-tagging and relatively simple spiking models to conclude that more excitable cells were biased IEG-tagging and identify potential mechanisms for identifying correlated engram activity. Our results are consistent with emerging literature and support a framework in which engrams are shaped by both existing hippocampal dynamics and inhibition.

Acknowledgements:
We would like to thank Jack Giblin, Kivilcim Kilic and the BU Neurophotonics Center for their training and support, and Joseph Zaki for helpful discussion of analyses. Denise Cai and Michael Hasselmo provided valuable comments. AM was supported by an NSF NRT award and an NIH DSPAN award. BBS was supported by a Young Investigator award from the BBRF and by a SEED

grant from the BU Neurophotonics Center. CL was supported by a Center for Systems Neuroscience Distinguished Postdoctoral Fellowship. This material is based upon work supported by an NIH Early Independence Award DP5 OD023106-01, NIH Transformative Award, Air Force Office of Scientific Research (AFOSR; FA9550-21-1-0310), the Ludwig Family Foundation, the Pew Scholars Program in the Biomedical Sciences, the Chan-Zuckerberg Initiative, and the Center for Systems Neuroscience and Neurophotonics Center at Boston University.

Author contributions:
Experiment design: AM, SR, BBS
Mouse imaging & behavioral experiments: AM, SC
In vivo data analysis: AM, SC
Model design & simulations: CL, GKO
Manuscript writing: AM, CL
Manuscript editing: AM, CL, BBS, SR, GKO

Declaration of Interest: The authors declare no competing interests.

Methods

Key Resources Table

Reagent or Resource	**Source**	**Identifier**
Experimental models: Organisms/strains		
C57BL/6J-Tg(Thy1-GCaMP6f)GP5.17Dkim/J	The Jackson Laboratory	Strain 025393
Bacterial and virus strains		
AAV9-c-fos-tTA-BGHpa	UMass Vector Core	Custom Ordered
AAV9-TRE-mCherry	UMass Vector Core	Custom Ordered
Chemicals, peptides and recombinant proteins		
Doxycycline diet (40 mg/kg)	Bio-Serv	Custom ordered dose
Software and algorithms		
Python 3.10	Python Software Foundation	https://www.python.org/
Arduino	Arduino	https://www.arduino.cc/

CellReg	Sheintuch et al. 2017 214/16/24 12:36:00 PM	https://github.com/flatironinstitute/CaImAn
CaImAn	Giovanucci et al 2019 574/16/24 12:36:00 PM	https://github.com/zivlab/CellReg
ImageJ (FIJI)	National Institutes of Health	https://fiji.sc/
FreezeFrame4	Actimetrics, Lafayette, IN	https://actimetrics.com/

Detailed Methods

Animals & Handling

Transgenic Thy1-GCaMP6f[58] (C57BL/6J-Tg(Thy1-GCaMP6f)GP5.17Dkim/J, Jackson Labs #025393, 16-24 weeks) were group housed with littermates prior to experiment start and given food and water *ad libitum.* The animal vivarium was maintained on a 12:12-hour light cycle (0700-1900). Following surgery, mice were single-housed to prepare for imaging experiments. All subjects were treated in accord with protocol 201900084 approved by the Institutional Animal Care and Use Committee (IACUC) at Boston University. Prior to imaging experiments, mice were habituated for 5 days to head-fixation.

Stereotaxic Surgery & Window Implantation

For all surgeries, mice were initially anesthetized with 3.0% isoflurane inhalation during induction and maintained at 1.5%–2% isoflurane inhalation through stereotaxic nose-cone delivery (oxygen 1L/min). Ophthalmic ointment (Systane) was applied to the eyes to provide adequate lubrication and prevent corneal desiccation. The hair on the scalp above the surgical site was removed using Veet hair removal cream and subsequently cleaned with alternating applications of betadine solution and 70% ethanol. 2.0% lidocaine hydrochloride was topically applied as local analgesia prior to midsagittal incision using an 11 blade scalpel of the scalp skin to expose the skull. A 0.1 mg/kg intraperitoneal (IP) dose of buprenorphine was administered at the beginning of surgery. A unilateral craniotomy was performed with a .5mm drillbit for viral injection. A 10 uL Hamilton syringe with an attached 33-gauge beveled needle was slowly lowered to the coordinates of dorsal CA1: -2.0 AP, +1.5ML -1.5 DV. 400 nL of 1:1 cocktail of AAV9-cFos-tTA/AAV9-TRE-mCherry (UMass Vector Core, titer $1x10^{13}$ GC/mL) was injected at a rate of 100 nL/min. The needle was allowed to rest at the injection site for 1-2 min prior to and after injection. Incisions were sutured closed using 4/0 Non-absorbable Nylon Monofilament Suture (Matrix Wizard). Following surgery, mice were injected with a 5 mg/kg intraperitoneal (IP) dose of ketoprofen. They were placed in a recovery cage with a heating pad until fully recovered from anesthesia. Histological assessment verified spread of dorsal CA1 viral targeting.

Seven to ten days later, a second surgery was performed to implant a hippocampal window for two-photon imaging. Prior to surgery, dexamethasone (3 mg/kg) was administered IP to aid brain swelling and inflammation. A 3mm craniotomy was created centered at the site of viral injection. Dura was peeled back with a bent 27-gauge needle tip. Cortical tissue washed with sterile saline

while aspirated using constant suction attached to 25-30 gauge needle tips. Tissue was aspirated down to white matter and corpus callosum fibers were carefully removed, leaving alveolar fibers intact. Blood was constantly removed via aspiration and absorption with saline-soaked hemostatic collagen sponge (Goodwill Hemosponge Absorbable Gelatin Sponge).

For the window implant, a 3mm diameter, 1.5mm deep stainless steel circular cannula (Ziggy's Tubes & Wires) was affixed to a 3 mm glass coverslip (#1 thickness, Thomas Scientific 1217N66) using UV curable optical adhesive (Norland). The cannula window was lowered carefully into the craniotomy site and Vetbond was used to adhere the edges of the cannula to the skull. The scalpel and drillbit was used to hatch the skull surface for best adhesion to the headplate. A custom stainless steel kinematic headplate[20] was affixed to the skull with the cannula centered using Metabond (Parkell). Mice were allowed to recover at least 1 week prior to handling & imaging took place 2 weeks after surgery.

Two-photon Imaging

All imaging was performed on a Bruker Ultima Investigator in Prairie View (v5.4). Excitation was delivered with a tunable Ti:Sapphire laser (Insight X3, Spectra Physics) at wavelengths of 920nm or 1040 nm and a primary dichroic (700 SP) split excitation and fluorescence light and a 770 SP IR blocker ensured no laser power reached the PMTs. On each imaging day, image series were collected at a frame rate of 30Hz with resonant galvos and resolution of 512x512 pixels. All imaging was with a 16x Nikon (3.0 mm, 0.8 NA) water immersion objective. Laser power was controlled with an electro-optic modulator (Conoptics 305-105-20) and post objective power ranged from 10-80 mW and did not exceed 100 mW. Emitted fluorescence was split into red and green channels with an emission filter cube set (565 LP dichroic, 525/70 for the green channel and 595/50 for red) and detected with two PMTs, for green (Hammamatsu H10770PB-40) and red (Hammamatsu H10770PB-50) channels. For recording spontaneous activity, 1-2 FOVs were recorded per animal for 22 minutes on Day 0 and Day 4 at 920nm. 1 FOV was excluded from 5 out of 12 mice due to either unreliable cell registration or resonant galvo image artifacts. For recording dual color GCaMP/TRE-mCherry expression, the same FOVs were recorded for ~1 minute (2000 frames) at a wavelength of 1040 nm. All dual color data was recorded at identical power settings on Day 0 and Day 4 in order to characterize mCherry fluorescence change across days.

During imaging mice were placed on a custom rotating disk that enabled them to locomote. A kinematic headplate and mount system was custom designed to ensure reliable registration of imaging FOV day to day and allowed for locomotion.[20] 4/16/24 12:36:00 PMThe imaging apparatus consisted of the kinematic mount held in place with ½" Thorlabs posts above a horizontal running disk. The rotating acrylic disk was 7" in diameter and a soft rubber adhesive was used to provide the mice traction for running on the disk. The center of the disk was screwed into an adjustable collar (McMaster Carr 9410T1) and mounted on a rotary encoder (US Digital H1-5000-IE-D) to measure running. A custom arduino script was used to record and synchronize image acquisition with running data from the disk. Wheel data was recorded in 9 of 12 mice.

Running behavior

To collect locomotion data, an arduino script was used to record timestamped positional data from the mouse's running disk. Timestamps were aligned to imaging frames by interpolating wheel

positional data with known frame times from Prairie View xml metadata files. To determine walking/running epochs, a velocity threshold of 1 cm/s was imposed to select for frames in which the animal was moving. Run epochs were selected requiring that the animal be greater than one for longer than 1 second and rest epochs were selected requiring the animal to be still for at least 1 second.

Fear Conditioning Tagging and Behavior

Prior to surgeries, mice were placed on a special diet of doxycycline chow (40 mg/kg, BioServ). When dox chow was removed (end of D0), this opened the window for activity-dependent viral labeling during the tagging period. For tagging, HC mice remained untouched in the home cages, while FC mice were placed in a conditioning chamber with plexiglass walls and a grid floor (17.78 cm L × 17.78 cm W × 30.48 cm H; Coulbourn Instruments) for a 7-minute conditioning session. Grid floors were connected to precision shockers and delivered a series of three footshocks (2 s, 1.0 mA intensity) at times 200s, 280s and 360s. Immediately after fear conditioning, the doxycycline diet was replaced in all mice cages immediately after tagging and mice remained on doxycycline diet for the duration of the imaging protocol (until after Day 4). Dox was removed after the conclusion of imaging sessions to allow full expression of tet-driven mCherry and check for injection spread (data not shown). For fear conditioning, video data were collected via overhead cameras (Computar) that interface with FreezeFrame (Actimetrics). FreezeFrame was used to control delivery of the foot shocks and perform freezing analyses. Freezing during fear conditioning was defined as bouts of 1.25 s or longer with minimal changes in pixel luminance.

Calcium deconvolution and event rates

All dF/F traces underwent calcium deconvolution to infer discrete event times. For event detection we utilized an L0 penalty method described in.[59,60] Briefly, each cell's dF/F trace is modeled as a noisy readout of underlying calcium fluorescence dynamics. Two parameters are used to fit event times to each cell's trace: gamma and lambda. Gamma is determined by the half-life of the indicator which we set to 0.14 s as reported for the Thy1-GCaMP6f GP.5.17 line.[58] Lambda controls the strictness of the L0 penalty and therefore the sparseness of events, with higher lambda values resulting in higher sparsity. We estimated lambda for each cell similarly to previous reports[61] and adjusted the minimum event size to 5 standard deviations of the noise in the dF/F of each cell. This threshold was chosen based on manual inspection of deconvolved traces with lower SNR and sparser activity. Mean event rates were calculated using the weighted sum of deconvolved event sizes, in order to account for calcium transients with larger amplitude as follows. For each cell, all detected calcium events had an associated non-zero magnitude, which were summed over the course of each imaging session and divided by total session time. This ensured smaller transients were not treated the same as larger transients when determining calcium event rate.

Correlation analyses

Deconvolved traces for cells were binned into overlapping 4 frame bins and pairwise Spearman correlations between every pair of cells simultaneously recorded were performed. Only cells active in both Day 0 and Day 4 sessions were used for this analysis. Pairwise correlations were grouped by cell identity and the mean correlation coefficient for all engram/engram, engram/non-

engram or non-engram/engram was calculated for each animal. For Supplementary Figure 5C-D, the correlations were calculated for bin sizes of 8, 10,16,20,25,32,40, 50, 64, 80, 100, and 125 frames. To evaluate if Spearman coefficients were statistically greater than zero, we performed a shuffle of our traces. We circularly shuffled all cells' traces independently 500 times and calculated the mean pairwise correlation between each population (engram/engram, engram/non-engram, non-engram/non-engram). For Supplementary Figure 5E-F, the upper 20% of pairwise correlations was used to define highly correlated pairs.

Spiking Network Model of CA3-CA1

We model each neuron's spike train as a Poisson process with time dependent rate $r_i(t)$ given by

$$r_i(t) = \phi(\sum_j G_{ij} * \frac{dN_j}{dt}(t)) + E_i(t)) \quad (1)$$

Here, $N_j(t)$ counts the total number of spikes neuron j has fired up to time t, and its derivative $\frac{dN_j}{dt} = \sum_k \delta(t - {t_j}^k)$ describes the neuron's spike train as a sum of Dirac delta functions. G is a matrix of synaptic interaction filters, and $*$ denotes a convolution, i.e. $(g * f)(t) = \int_{t_0}^{\infty} dt'\, g(t - t')f(t')$. We take $G_{ij}(s) = J_{ij} \frac{1}{\tau} exp\,(-s/\tau)$ (for $s \geq 0$) where J_{ij} gives the synaptic weight from neuron j onto neuron i. We take ϕ to be threshold-quadratic, i.e. $\phi(x) = max(x, 0)^2$.

Our synaptic weight matrices were constructed to reflect recurrent E-E connectivity in CA3, as well as recurrent E-I connectivity in both CA1 and CA3 and feedforward connectivity from CA3 to CA1 (Figure 5A). We base our weight matrix J on the connectivity of regions CA1 and CA3 of the hippocampus. We further subdivide both CA1 and CA3 into excitatory engram neurons (E), excitatory non-engram neurons (N), and inhibitory neurons (I). The regional connectivity is given by a 6x6 matrix $\bar{J}$.

$$\bar{J} = J_0 \begin{array}{c} \begin{matrix} CA3E & CA3N & CA3I & CA1E & CA1N & CA1I \end{matrix} \\ \begin{pmatrix} h & 1 & -h_{I3}g & 0 & 0 & 0 \\ 1 & 1 & -g & 0 & 0 & 0 \\ 1 & 1 & -g_{II} & 0 & 0 & 0 \\ h & 1 & 0 & 0 & 0 & -h_{I1}g \\ 1 & 1 & 0 & 0 & 0 & -g \\ 1 & 1 & 0 & 1 & 1 & -g_{II} \end{pmatrix} \end{array} \begin{matrix} CA3E \\ CA3N \\ CA3I \\ CA1E \\ CA1N \\ CA1I \end{matrix}$$

Here, the parameter h describes the strength of engram to engram synapses relative to the baseline strength of excitatory to excitatory synapses, the parameter g describes the relative strength of inhibitory to excitatory connections, the parameter g_{II} describes the relative strength of inhibitory to inhibitory synapses, and the parameters h_{I3} and h_{I1} describe the strength of the homeostatic inhibitory plasticity, i.e. the increased inhibition recruited by engram cells, in CA3 and CA1, respectively.

Neuron to neuron connectivity is described by a block-wise Erdős-Rényi adjacency matrix A, with sparse excitatory connectivity and dense inhibitory connectivity given by $p_{EE} = 0.1, p_{IE} =$

$0.8, p_{II} = 0.8, p_{EI} = 0.8$. The connection probabilities do not differ between engram and non-engram cells. Finally, the neuron-to-to neuron weights J_{ij} are given by $J_{ij} = \frac{A_{ij}}{N_{\alpha(j)} p_{\alpha(i)\alpha(j)}} \bar{J}_{\alpha(i)\,\alpha(j)}$ where $\alpha(i)$ gives the region containing neuron i.

Estimating population rates and correlations

In addition to using our stochastic spiking model to simulate neural activity, we calculate estimates for the expected firing rate r_i of each neuron as well as the expected correlation C_{ij} between each pair of neurons. For more details, see [62–64]. To find a self-consistent equilibrium rate r_i for each neuron, we substitute r_j for $\frac{dN_j}{dt}$ in Equation 1 and replace convolution with G_{ij} with multiplication by J_{ij} because the expected rate r_j is constant. We then find r by numerically solving

$$r = \phi(J r + E).$$

In addition to finding the individual expected rate for each neuron for a fixed neuron-level connectivity matrix J, we can find the expected rate of a neuron in each population, where the expectation is taken both over the random connectivity matrix J and the stochastic spiking. Letting $\bar{r}$ denote the vector of expected rates for each population and $\bar{E}$ denote the mean input to each population, we have

$$\bar{r} = \phi(\bar{J}\bar{r} + \bar{E})$$

We again solve this numerically to find $\bar{r}$. Note that these estimates are all for the mean-field rate, i.e. they do not include corrections to the firing rate resulting from correlations in the input interacting with the nonlinear function ϕ. To account for this, we add a one-loop correction term.[65]

To estimate the expected spike train covariance matrix Σ, we linearize around the expected rate and apply the formula

$$\Sigma = \Delta R \Delta^T$$

where $\Delta = (I - \phi'(r) J)^{-1}$, R is a diagonal matrix with $R_{ii} = r_i$, and $\phi'(r)$ is a diagonal matrix with $\phi'(r)_{ii} = \phi'(r_i)$. We then compute the correlation matrix C from the covariance matrix Σ by $C_{ij} = \frac{\Sigma_{ij}}{\sqrt{\Sigma_{ii}\Sigma_{jj}}}$.

As with the rate, we also estimate the expected value for the population-level correlation, i.e. the matrix $\bar{C}$ with entries $\overline{C_{\alpha\beta}}$ giving the expected correlation between a neuron in population α and a neuron in population β where the expectation is taken over both the random connectivity matrix J and the stochastic spiking. Letting $\overline{\Sigma_{\alpha\beta}}$ denote our estimate of the expected covariance between a neuron in population α and a (distinct) neuron in population β, we have

$$\bar{\Sigma} = \bar{\Delta} N^{-1} \bar{R} \bar{\Delta}^T - N^{-1} \bar{R}.$$

Here, we define $\bar{\Delta} = (I - \phi'(\bar{r}) \bar{J})^{-1}$ and use N to denote the diagonal matrix with $N_{\alpha\alpha}$ giving the number of neurons in population α.

For each population, we can also compute the expected variance of a neuron, which is given by

$\overline{\sigma_\alpha} = \overline{\Sigma_{\alpha\alpha}} + \bar{r_\alpha}$Finally, we compute the population correlation matrix $\bar{C}$ by $\overline{C_{\alpha\beta}} = \frac{\overline{\Sigma_{\alpha\beta}}}{\overline{\sigma_\alpha}\,\overline{\sigma_\beta}}$.

Simulating noisy tagging, homeostatic inhibitory plasticity, and increased inhibition

In Figure 5G and H, we introduce noisy tagging into our model. We fix the percentage of engram cells in our model at 50%, and include a false tagging probability p_{FP}, giving the probability that each non-engram cell gets tagged as an engram cell, i.e. $p(tagged|engram)$. We do not include any false negative tagging, i.e. we assume every engram cell gets appropriately tagged. We then investigate how noisy tagging can obscure any increase in engram rates and correlations following learning. The observed rate of the tagged cells is calculated as a weighted average of the true engram rate and the non-engram rate, i.e.

$$r_{obs} = p(engram \mid tagged) r_{engram} + p(non-engram|tagged)\, r_{non-engram.}$$

where $p(engram \mid tagged)$ and $p(non-engram|tagged)$ are calculated via Bayes theorem and r_{engram}, $r_{non-engram.}$ are calculated in the baseline model with no noisy tagging.
The observed tagged-tagged correlation is likewise calculated as

$$c_{obs} = p(engram \mid tagged)^2 c_{EE} + p(engram|tagged)\, p(non-engram|tagged)\, c_{EN} + p(non-engram|tagged)^2 c_N.$$

We include homeostatic inhibitory plasticity into our model and show that it is capable of controlling the increase in rates following learning. In Figure 5C (left side), for each level of engram to engram connectivity h, we use grid search with our population level prediction of the rate to find the value of h_{I3} for which the predicted CA3 engram rates match their baseline before learning (h = 1) value. Then, using this value of h_{I3}, we repeat the same procedure for CA1 in order to find the value of h_{I1} which ensures that the CA1 engram rates match their baseline before learning value. On the right side of Figure 5C, we show that the values of h_{I3} and $h_{I3\ we}$ found this way are able to control the increase in engram rates following learning. Homeostatic inhibitory plasticity is included in all model figures except Figure 5B and 5H.

In Figure 5E and F, we explore the role of increased baseline inhibition in controlling the change in correlations following learning. To make comparisons across models with different levels of inhibition, we increase the input to the excitatory neurons to keep the baseline rates constant for all levels of inhibition.

Image Processing and ROI Extraction

Images were first spatially resized in Fiji (method: averaging, bilinear interpolation) to 256x256 (1.58 um/pixel resolution). All image processing was done using custom Python scripts using the CaImAn python package[57] https://github.com/flatironinstitute/CaImAn). Images were first motion corrected using NoRMCorre with non-rigid motion correction implemented in CaImAn. Day 4 images were registered to the average template image from Day 0 so cellular ROIs to allow for in alignment across days. Similarly, two-color images (1040 nm time series) were aligned to the 920nm functional images as follows. 1040 nm green channel images were motion corrected to

the 920 nm GCaMP average image template and these shifts were applied to the 1040 nm red channel images in order to align green/red channels with the ROIs extracted on the 920 nm images. In some cases, the red channel images were motion corrected to the Day 0 average red channel image template and shifts were applied to the green channel. After motion correction, CNMF was used to extract cellular ROIs and dF/F traces. Registration of cell ROIs across days was performed with the CellReg MATLAB GUI.[21] Visual inspection of spatial ROIs and cell registration was performed, and inaccurate spatial ROIs were excluded. For this step, first CellReg output was visualized as a whole with color coded ROIs for registered cells (Supplementary Figure 2A). Next, each ROI pair was plotted on top of the session's mean template image and correlation image (calculated with CaImAn's '*caiman.summary_images.local_correlations*' function) and manually verified as a true registered cell pair (Supplementary Figure 2B). Additionally, ROIs with a SNR less than 4 were discarded based on visual inspection of lower SNR traces. We did this by thresholding ROIs using CaImAns SNR metric for each ROI from '*cnmf.estimates.SNR_comp*'. Cell ROIs were then manually classified as engram or non-engram based on user-picked threshold of mCherry intensity and visual evaluation of their mCherry expression on Day 4, taking into account the soma intensity relative to the local background of each cell (Figure 1D, see mCherry expression analyses below).

mCherry expression analyses

Analysis of mCherry expression was done on averaged red channel images collected at 1040 after the two-color registration described above. To calculate relative local mCherry expression (Figure 1D), cell ROI coordinates were scaled by a factor of 1.5 around the center of mass for each cell ROI. Expression within each ROI was subtracted from this larger ROI and a ratio of fluorescence in the local background surrounding the cell ROI to fluorescence within the ROI was calculated. To calculate fold change (Supplementary Figure 1D), raw mCherry fluorescence was measured in registered cell ROIs on Day 0 and Day 4 and D4 mean intensity was divided by D0 mean intensity.

To account for leak in doxycycline suppression of the TetTag constructs, we removed high-expressing mCherry cells on D0 from our engram population, which represented 2 percent of our active CA1 population (Supplementary Figure 1A,E). This was done by removing Day 0 cells with expression greater than 2.5 standard deviations from the mean ROI intensity from the classified engram population. Importantly, we observed a robust increase in overall mCherry fluorescence from D0 to D4 (Supplementary Figure 1B-C), suggesting widespread mCherry tagging during the period of Dox removal. However, this increase was observed across all cells (Supplementary Figure 1B). Given this, we decided to classify engram cells by choosing a threshold of mCherry cell intensity on Day 4 and manually evaluating these thresholds, taking into account a cell's expression of mCherry relative to its local background (Figure 1C-D). This approach was validated by calculating the ratio of somatic mCherry to its local background and engram cells had increased a higher relative fluorescence of mCherry (Figure 1D). In addition, engram-classified cells demonstrated an overall higher raw mCherry fluorescence intensities (Supplementary Figure 1C) and fold change in mCherry expression from D0 to D4 (Supplementary Figure 1D), suggesting a greater change in Fos driven fluorescence during the tagging window.

Statistical analysis

All statistical analyses were performed in Python using the statistical package pingouin (v0.5.3) or statsmodels (v0.13.5). Normality tests were performed to determine the appropriate statistical testing. For comparing across groups and time, 2-Way Repeated Measures ANOVAS were conducted with subsequent post hoc analyses (paired or unpaired t-tests for parametric data and Wilcoxon signed-rank tests or Mann-Whitney U tests for non-parametric data), corrected for multiple comparisons (Bonferroni's correction). Data are shown as mean +/- sem and for regressions 95% confidence intervals are shown.

References

1. Josselyn, S.A., Köhler, S., and Frankland, P.W. (2015). Finding the engram. Nat Rev Neurosci *16*, 521–534. 10.1038/nrn4000.
2. Josselyn, S.A., and Tonegawa, S. (2020). Memory engrams: Recalling the past and imagining the future. Science *367*. 10.1126/science.aaw4325.
3. Eichenbaum, H. (2017). On the Integration of Space, Time, and Memory. Neuron *95*, 1007–1018. 10.1016/j.neuron.2017.06.036.
4. Denny, C.A., Kheirbek, M.A., Alba, E.L., Tanaka, K.F., Brachman, R.A., Laughman, K.B., Tomm, N.K., Turi, G.F., Losonczy, A., and Hen, R. (2014). Hippocampal memory traces are differentially modulated by experience, time, and adult neurogenesis. Neuron *83*, 189–201. 10.1016/j.neuron.2014.05.018.
5. Liu, X., Ramirez, S., Pang, P.T., Puryear, C.B., Govindarajan, A., Deisseroth, K., and Tonegawa, S. (2012). Optogenetic stimulation of a hippocampal engram activates fear memory recall. Nature *484*, 381–385. 10.1038/nature11028.
6. Ramirez, S., Liu, X., Lin, P.-A., Suh, J., Pignatelli, M., Redondo, R.L., Ryan, T.J., and Tonegawa, S. (2013). Creating a False Memory in the Hippocampus. Science *341*, 387–391. 10.1126/science.1239073.
7. Shpokayte, M., McKissick, O., Guan, X., Yuan, B., Rahsepar, B., Fernandez, F.R., Ruesch, E., Grella, S.L., White, J.A., Liu, X.S., et al. (2022). Hippocampal cells segregate positive and negative engrams. Commun Biol *5*, 1009. 10.1038/s42003-022-03906-8.
8. Chen, B.K., Murawski, N.J., Cincotta, C., McKissick, O., Finkelstein, A., Hamidi, A.B., Merfeld, E., Doucette, E., Grella, S.L., Shpokayte, M., et al. (2019). Artificially Enhancing and Suppressing Hippocampus-Mediated Memories. Current Biology, 1–10. 10.1016/j.cub.2019.04.065.
9. Grella, S.L., Fortin, A.H., Ruesch, E., Bladon, J.H., Reynolds, L.F., Gross, A., Shpokayte, M., Cincotta, C., Zaki, Y., and Ramirez, S. (2022). Reactivating hippocampal-mediated memories during reconsolidation to disrupt fear. Nat Commun *13*, 4733. 10.1038/s41467-022-32246-8.
10. Zhou, Y., Zhu, H., Liu, Z., Chen, X., Su, X., Ma, C., Tian, Z., Huang, B., Yan, E., Liu, X., et al. (2019). A ventral CA1 to nucleus accumbens core engram circuit mediates conditioned place preference for cocaine. Nat Neurosci *22*, 1986–1999. 10.1038/s41593-019-0524-y.
11. Tanaka, K.Z., He, H., Tomar, A., Niisato, K., Huang, A.J.Y., and McHugh, T.J. (2018). The hippocampal engram maps experience but not place. Science *361*, 392–397. 10.1126/science.aat5397.

12. Pettit, N.L., Yap, E.-L., Greenberg, M.E., and Harvey, C.D. (2022). Fos ensembles encode and shape stable spatial maps in the hippocampus. Nature. 10.1038/s41586-022-05113-1.
13. Chen, L., Cummings, K.A., Mau, W., Zaki, Y., Dong, Z., Rabinowitz, S., Clem, R.L., Shuman, T., and Cai, D.J. (2020). The role of intrinsic excitability in the evolution of memory: Significance in memory allocation, consolidation, and updating. Neurobiology of Learning and Memory *173*, 107266. 10.1016/j.nlm.2020.107266.
14. Josselyn, S.A., and Frankland, P.W. (2018). Memory Allocation: Mechanisms and Function. Annual Review of Neuroscience *41*, 389–413. 10.1146/annurev-neuro-080317-061956.
15. Tanaka, K.Z., Pevzner, A., Hamidi, A.B., Nakazawa, Y., Graham, J., and Wiltgen, B.J. (2014). Cortical Representations Are Reinstated by the Hippocampus during Memory Retrieval. Neuron *84*, 347–354. 10.1016/j.neuron.2014.09.037.
16. Ghandour, K., Ohkawa, N., Fung, C.C.A., Asai, H., Saitoh, Y., Takekawa, T., Okubo-Suzuki, R., Soya, S., Nishizono, H., Matsuo, M., et al. (2019). Orchestrated ensemble activities constitute a hippocampal memory engram. Nat Commun *10*, 2637. 10.1038/s41467-019-10683-2.
17. Ryan, T.J., Roy, D.S., Pignatelli, M., Arons, A., and Tonegawa, S. (2015). Engram cells retain memory under retrograde amnesia. Science *348*, 1007–1013. 10.1126/science.aaa5542.
18. Castello-Waldow, T.P., Weston, G., Ulivi, A.F., Chenani, A., Loewenstein, Y., Chen, A., and Attardo, A. (2020). Hippocampal neurons with stable excitatory connectivity become part of neuronal representations. PLoS Biol *18*, e3000928. 10.1371/journal.pbio.3000928.
19. Choi, J.H., Sim, S.E., Kim, J. il, Choi, D.I.I., Oh, J., Ye, S., Lee, J., Kim, T.H., Ko, H.G., Lim, C.S., et al. (2018). Interregional synaptic maps among engram cells underlie memory formation. Science *360*, 430–435. 10.1126/science.aas9204.
20. Kim, S.J., Slocum, A.H., and Scott, B.B. (2022). A miniature kinematic coupling device for mouse head fixation. Journal of Neuroscience Methods *372*, 109549. 10.1016/j.jneumeth.2022.109549.
21. Sheintuch, L., Rubin, A., Brande-Eilat, N., Geva, N., Sadeh, N., Pinchasof, O., and Ziv, Y. (2017). Tracking the Same Neurons across Multiple Days in Ca2+ Imaging Data. Cell Reports *21*, 1102–1115. 10.1016/j.celrep.2017.10.013.
22. Ocker, G.K., and Doiron, B. (2019). Training and Spontaneous Reinforcement of Neuronal Assemblies by Spike Timing Plasticity. Cerebral Cortex *29*, 937–951. 10.1093/cercor/bhy001.
23. Chen, L., Li, X., Tjia, M., and Thapliyal, S. (2022). Homeostatic plasticity and excitation-inhibition balance: The good, the bad, and the ugly. Current Opinion in Neurobiology *75*, 102553. 10.1016/j.conb.2022.102553.
24. Yiu, A.P., Mercaldo, V., Yan, C., Richards, B., Rashid, A.J., Hsiang, H.-L.L., Pressey, J., Mahadevan, V., Tran, M.M., Kushner, S.A., et al. (2014). Neurons Are Recruited to a Memory Trace Based on Relative Neuronal Excitability Immediately before Training. Neuron *83*, 722–735. 10.1016/j.neuron.2014.07.017.
25. Rashid, A.J., Yan, C., Mercaldo, V., Hsiang, H.L., Park, S., Cole, C.J., De Cristofaro, A., Yu, J., Ramakrishnan, C., Lee, S.Y., et al. (2016). Competition between engrams influences fear memory formation and recall. Science *353*. 10.1126/science.aaf0594.

26. Zhou, Y., Won, J., Karlsson, M.G., Zhou, M., Rogerson, T., Balaji, J., Neve, R., Poirazi, P., and Silva, A.J. (2009). CREB regulates excitability and the allocation of memory to subsets of neurons in the amygdala. Nat Neurosci *12*, 1438–1443. 10.1038/nn.2405.
27. Park, S., Kramer, E.E., Mercaldo, V., Rashid, A.J., Insel, N., Frankland, P.W., and Josselyn, S.A. (2016). Neuronal Allocation to a Hippocampal Engram. Neuropsychopharmacology *41*, 2987–2993. 10.1038/npp.2016.73.
28. Mocle, A.J., Ramsaran, A.I., Jacob, A.D., Rashid, A.J., Luchetti, A., Tran, L.M., Richards, B.A., Frankland, P.W., and Josselyn, S.A. (2024). Excitability mediates allocation of pre-configured ensembles to a hippocampal engram supporting contextual conditioned threat in mice. Neuron, S0896627324000916. 10.1016/j.neuron.2024.02.007.
29. Cai, D.J., Aharoni, D., Shuman, T., Shobe, J., Biane, J., Song, W., Wei, B., Veshkini, M., La-Vu, M., Lou, J., et al. (2016). A shared neural ensemble links distinct contextual memories encoded close in time. Nature *534*, 115–118. 10.1038/nature17955.
30. Zaki, Y., Pennington, Z.T., Morales-Rodriguez, D., Francisco, T.R., LaBanca, A.R., Dong, Z., Lamsifer, S., Segura, S.C., Chen, H.-T., Christenson Wick, Z., et al. (2023). Aversive experience drives offline ensemble reactivation to link memories across days (Neuroscience) 10.1101/2023.03.13.532469.
31. Chen, L., Francisco, T.R., Baggetta, A.M., Zaki, Y., Ramirez, S., Clem, R.L., Shuman, T., and Cai, D.J. (2023). Ensemble-specific deficit in neuronal intrinsic excitability in aged mice. Neurobiology of Aging *123*, 92–97. 10.1016/j.neurobiolaging.2022.12.007.
32. Joo, H.R., and Frank, L.M. (2018). The hippocampal sharp wave–ripple in memory retrieval for immediate use and consolidation. Nat Rev Neurosci *19*, 744–757. 10.1038/s41583-018-0077-1.
33. Yang, W., Sun, C., Huszár, R., Hainmueller, T., Kiselev, K., and Buzsáki, G. (2024). Selection of experience for memory by hippocampal sharp wave ripples.
34. Pastalkova, E., Itskov, V., Amarasingham, A., and Buzsáki, G. (2008). Internally Generated Cell Assembly Sequences in the Rat Hippocampus. Science *321*, 1322–1327. 10.1126/science.1159775.
35. Dragoi, G., and Tonegawa, S. (2011). Preplay of future place cell sequences by hippocampal cellular assemblies. Nature *469*, 397–401. 10.1038/nature09633.
36. Dragoi, G. (2024). The generative grammar of the brain: a critique of internally generated representations. Nat. Rev. Neurosci. *25*, 60–75. 10.1038/s41583-023-00763-0.
37. Suthard, R.L., Senne, R.A., Buzharsky, M.D., Diep, A.H., Pyo, A.Y., and Ramirez, S. (2024). Engram reactivation mimics cellular signatures of fear. Cell Reports *43*, 113850. 10.1016/j.celrep.2024.113850.
38. Cowansage, K.K., Shuman, T., Dillingham, B.C., Chang, A., Golshani, P., and Mayford, M. (2014). Direct Reactivation of a Coherent Neocortical Memory of Context. Neuron *84*, 432–441. 10.1016/j.neuron.2014.09.022.
39. Barron, H.C., Vogels, T.P., Behrens, T.E., and Ramaswami, M. (2017). Inhibitory engrams in perception and memory. Proc. Natl. Acad. Sci. U.S.A. *114*, 6666–6674. 10.1073/pnas.1701812114.
40. Sadeh, S., and Clopath, C. (2021). Inhibitory stabilization and cortical computation. Nat Rev Neurosci *22*, 21–37. 10.1038/s41583-020-00390-z.

41. Delamare, G., Tomé, D.F., and Clopath, C. (2024). Intrinsic neural excitability biases allocation and overlap of memory engrams. J. Neurosci., e0846232024. 10.1523/JNEUROSCI.0846-23.2024.
42. Morrison, D.J., Rashid, A.J., Yiu, A.P., Yan, C., Frankland, P.W., and Josselyn, S.A. (2016). Parvalbumin interneurons constrain the size of the lateral amygdala engram. Neurobiology of Learning and Memory *135*, 91–99. 10.1016/j.nlm.2016.07.007.
43. Yap, E.-L., Pettit, N.L., Davis, C.P., Nagy, M.A., Harmin, D.A., Golden, E., Dagliyan, O., Lin, C., Rudolph, S., Sharma, N., et al. (2021). Bidirectional perisomatic inhibitory plasticity of a Fos neuronal network. Nature *590*, 115–121. 10.1038/s41586-020-3031-0.
44. Reijmers, L.G., Perkins, B.L., Matsuo, N., and Mayford, M. (2007). Localization of a stable neural correlate of associative memory. Science *317*, 1230–1233. 10.1126/science.1143839.
45. Lucchetti, J., Fracasso, C., Balducci, C., Passoni, A., Forloni, G., Salmona, M., and Gobbi, M. (2019). Plasma and Brain Concentrations of Doxycycline after Single and Repeated Doses in Wild-Type and APP23 Mice. J Pharmacol Exp Ther *368*, 32–40. 10.1124/jpet.118.252064.
46. Robertson, A., Perea, J., Tolmachova, T., Thomas, P.K., and Huxley, C. (2002). Effects of mouse strain, position of integration and tetracycline analogue on the tetracycline conditional system in transgenic mice. Gene *282*, 65–74. 10.1016/S0378-1119(01)00793-4.
47. DeNardo, L.A., Liu, C.D., Allen, W.E., Adams, E.L., Friedmann, D., Fu, L., Guenthner, C.J., Tessier-Lavigne, M., and Luo, L. (2019). Temporal evolution of cortical ensembles promoting remote memory retrieval. Nat Neurosci *22*, 460–469. 10.1038/s41593-018-0318-7.
48. DeNardo, L., and Luo, L. (2017). Genetic strategies to access activated neurons. Current Opinion in Neurobiology *45*, 121–129. 10.1016/j.conb.2017.05.014.
49. Murthy, B.K.B., Somatakis, S., Ulivi, A.F., Klimmt, H., Castello-Waldow, T.P., Haynes, N., Huettl, R.E., Chen, A., and Attardo, A. (2023). Arc-driven mGRASP highlights CA1 to CA3 synaptic engrams. Front. Behav. Neurosci. *16*, 1072571. 10.3389/fnbeh.2022.1072571.
50. Hyun, J.H., Nagahama, K., Namkung, H., Mignocchi, N., Roh, S.-E., Hannan, P., Krüssel, S., Kwak, C., McElroy, A., Liu, B., et al. (2022). Tagging active neurons by soma-targeted Cal-Light. Nat Commun *13*, 7692. 10.1038/s41467-022-35406-y.
51. Jung, J.H., Wang, Y., Rashid, A.J., Zhang, T., Frankland, P.W., and Josselyn, S.A. (2023). Examining memory linking and generalization using scFLARE2, a temporally precise neuronal activity tagging system. Cell Reports *42*, 113592. 10.1016/j.celrep.2023.113592.
52. Sanchez, M.I., Nguyen, Q.-A., Wang, W., Soltesz, I., and Ting, A.Y. (2020). Transcriptional readout of neuronal activity via an engineered Ca^{2+} -activated protease. Proc. Natl. Acad. Sci. U.S.A. *117*, 33186–33196. 10.1073/pnas.2006521117.
53. Kim, C.K., Sanchez, M.I., Hoerbelt, P., Fenno, L.E., Malenka, R.C., Deisseroth, K., and Ting, A.Y. (2020). A Molecular Calcium Integrator Reveals a Striatal Cell Type Driving Aversion. Cell *183*, 2003-2019.e16. 10.1016/j.cell.2020.11.015.
54. Litwin-Kumar, A., and Doiron, B. (2014). Formation and maintenance of neuronal assemblies through synaptic plasticity. Nat Commun *5*, 5319. 10.1038/ncomms6319.
55. Ahmed, M.S., Priestley, J.B., Castro, A., Stefanini, F., Solis Canales, A.S., Balough, E.M., Lavoie, E., Mazzucato, L., Fusi, S., and Losonczy, A. (2020). Hippocampal Network

Reorganization Underlies the Formation of a Temporal Association Memory. Neuron *107*, 283-291.e6. 10.1016/j.neuron.2020.04.013.

56. Ratigan, H.C., Krishnan, S., Smith, S., and Sheffield, M.E.J. (2023). A thalamic-hippocampal CA1 signal for contextual fear memory suppression, extinction, and discrimination. Nat Commun *14*, 6758. 10.1038/s41467-023-42429-6.
57. Giovannucci, A., Friedrich, J., Gunn, P., Kalfon, J., Brown, B.L., Koay, S.A., Taxidis, J., Najafi, F., Gauthier, J.L., Zhou, P., et al. (2019). CaImAn an open source tool for scalable calcium imaging data analysis. eLife *8*, e38173. 10.7554/eLife.38173.
58. Dana, H., Chen, T.-W., Hu, A., Shields, B.C., Guo, C., Looger, L.L., Kim, D.S., and Svoboda, K. (2014). Thy1-GCaMP6 Transgenic Mice for Neuronal Population Imaging In Vivo. PLoS ONE *9*, e108697. 10.1371/journal.pone.0108697.
59. Jewell, S., and Witten, D. (2018). Exact spike train inference via ℓ_{0} optimization. Ann. Appl. Stat. *12*. 10.1214/18-AOAS1162.
60. Jewell, S.W., Hocking, T.D., Fearnhead, P., and Witten, D.M. (2020). Fast nonconvex deconvolution of calcium imaging data. Biostatistics *21*, 709–726. 10.1093/biostatistics/kxy083.
61. De Vries, S.E.J., Lecoq, J.A., Buice, M.A., Groblewski, P.A., Ocker, G.K., Oliver, M., Feng, D., Cain, N., Ledochowitsch, P., Millman, D., et al. (2020). A large-scale standardized physiological survey reveals functional organization of the mouse visual cortex. Nat Neurosci *23*, 138–151. 10.1038/s41593-019-0550-9.
62. HAWKES, A.G. (1971). Spectra of some self-exciting and mutually exciting point processes. Biometrika *58*, 83–90. 10.1093/biomet/58.1.83.
63. Pernice, V., Staude, B., Cardanobile, S., and Rotter, S. (2011). How Structure Determines Correlations in Neuronal Networks. PLoS Comput Biol *7*, e1002059. 10.1371/journal.pcbi.1002059.
64. Ocker, G.K., Hu, Y., Buice, M.A., Doiron, B., Josić, K., Rosenbaum, R., and Shea-Brown, E. (2017). From the statistics of connectivity to the statistics of spike times in neuronal networks. Current Opinion in Neurobiology *46*, 109–119. 10.1016/j.conb.2017.07.011.
65. Ocker, G.K., Josić, K., Shea-Brown, E., and Buice, M.A. (2017). Linking structure and activity in nonlinear spiking networks. PLoS Comput Biol *13*, e1005583. 10.1371/journal.pcbi.1005583.

FIGURES

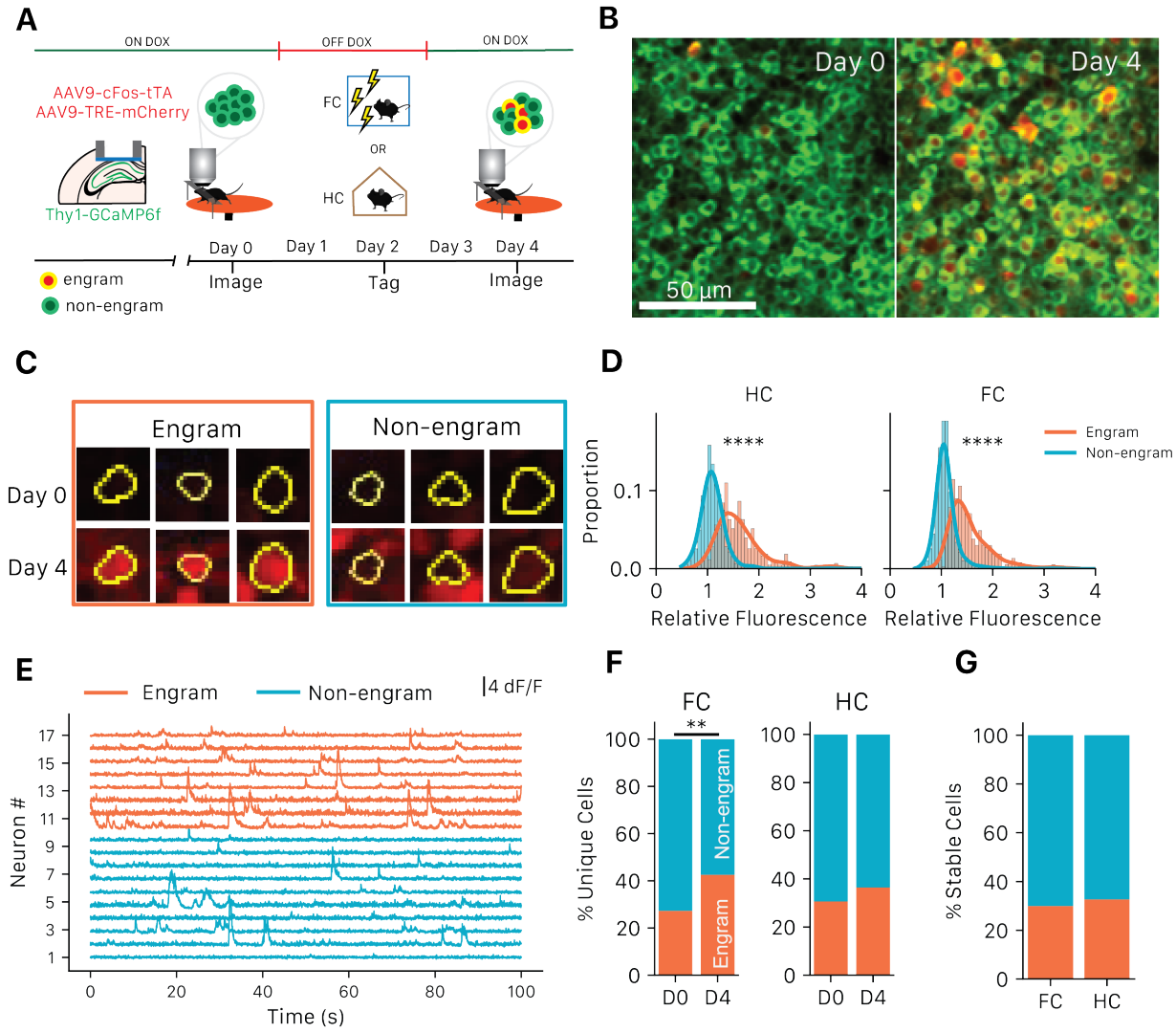

Figure 1. Imaging spontaneous activity in engram cells before and after learning

A) Experimental timeline. Doxyclicline (Dox) is removed after imaging on Day 0 to open mCherry tagging window. Mice are off dox Days 1-2 and either fear conditioned on Day 2 or remain in homecage. Dox is replaced on Day 2 and spontaneous imaging of the same CA1 population is repeated on Day 4.

B) Example dual color FOV before and after tagging.

C) Representative engram and non-engram cells before and after mCherry tagging.

D) Relative fluorescence of mCherry expression in engram vs non engram cells on Day 4 (engram vs non-engram cells: HC $p < 0.0001$, FC $p < 0.0001$)

E) Representative calcium traces of spontaneous activity in engram and non-engram cells

F) Percent of each cell type unique to each day. Percent Engram cells 2Way RM ANOVA Group x Session (Session $F= 24.53$, $p = 0.0006$, Interaction $F= 5.63$, $p=.039$, FC D0 vs D4 $p=0.0098$, HC D0 vs D4 $p=0.16$)

G) Percent of each cell type stably active on both days. (T-test FC vs HC T=-0.55, p=0.60)

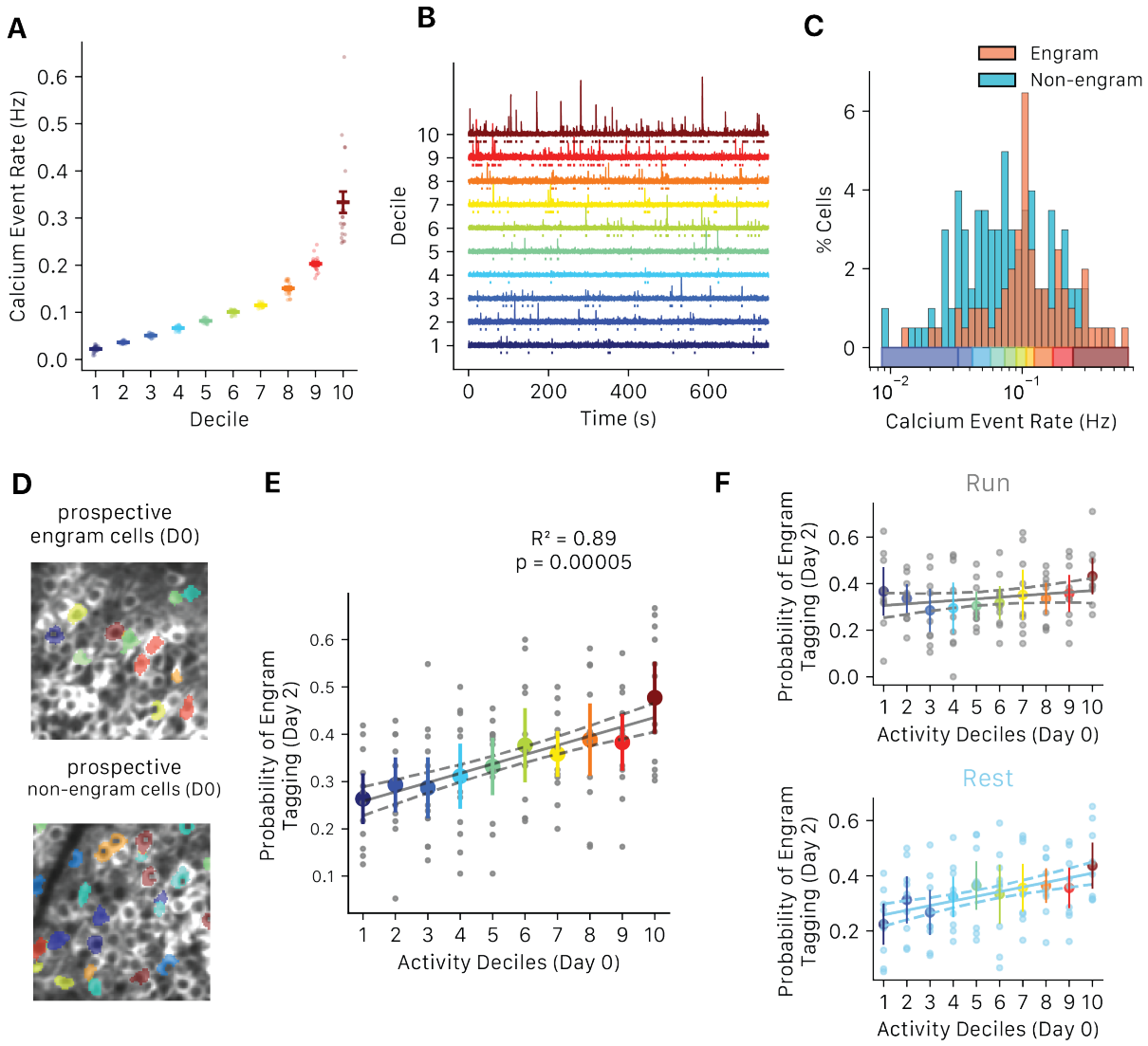

Figure 2. Day 0 spontaneous activity predicts engram allocation 1-2 days before tagging

A) Example cells of engram tagged (allocated) and non-tagged cells and their activity traces from Day 0.

B) Deciles of activity from representative Day 0 FC animal B) Example traces from cells in each activity decile

C) Histogram of activity rates of engram (blue) and non-engram (orange) cells overlaid over decile ranges (rainbow).

D) Footprints of prospective engram (top) or non-engram (bottom) cells. Spatial ROIs are colored by activity decile (same as Figure 2A-B). Cells in each decile are distributed spatially.

E) Baseline (Day 0) activity correlates with probability of engram allocation. Linear regression R^2 = 0.89, p = 0.00005, n=12 mice.

F) Baseline (Day 0) activity is correlated during periods of rest (bottom, blue) and not running (top, gray). Linear regression; Rest R^2 = 0.76, p=0.001, Run R^2 = 0.26, p=0.14, n=9 mice).

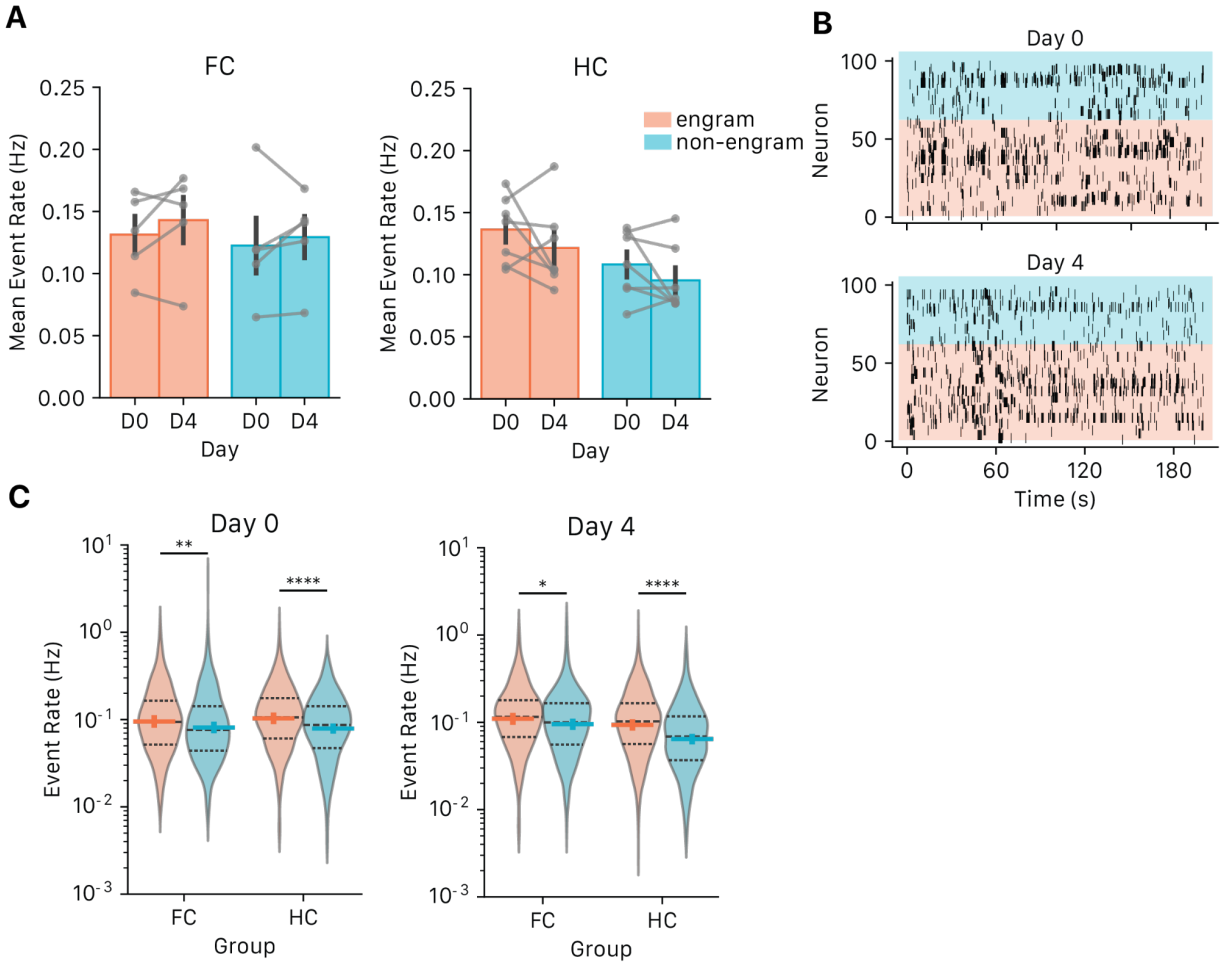

Figure 3. CA1 engram cell activity rates do not change with learning

A) Mean weighted event rates for FC (left, n=5) and HC (animals, n=7) across sessions do not change.

FC: 2 Way RM ANOVA, Population x Day (Population, F = 0.21 p = 0.66, Day F = 1.44 p = 0.27 Interaction F=0.10 p=.76; pairwise comparisons D0 vs D4 Engram p = 0.65, Non-engram p = 1.0)

HC: 2 Way RM ANOVA, Population x Day (Population, F = 4.36 p = 0.06, Day F = 2.73 p = 0.12, Interaction F=0.014 p=0.91; pairwise comparisons D0 vs D4 Engram p = 0.63, Non-engram p = 0.48)

C) Example raster plots of calcium events in engram (orange) and non-engram (teal) cells on Day 0 and Day 4.

D) Violin plots of distribution of all engram vs non-engram cell event rates (Mann-Whitney U-test D0: FC U = 75781.0, p = 0.004, HC U = 132990.0 p = 3e-6; D4: FC U = 78668.0 p = 0.043, HC U = 123755.0 p = 2e-10, n= 839 FC cells, 1175 HC cells)

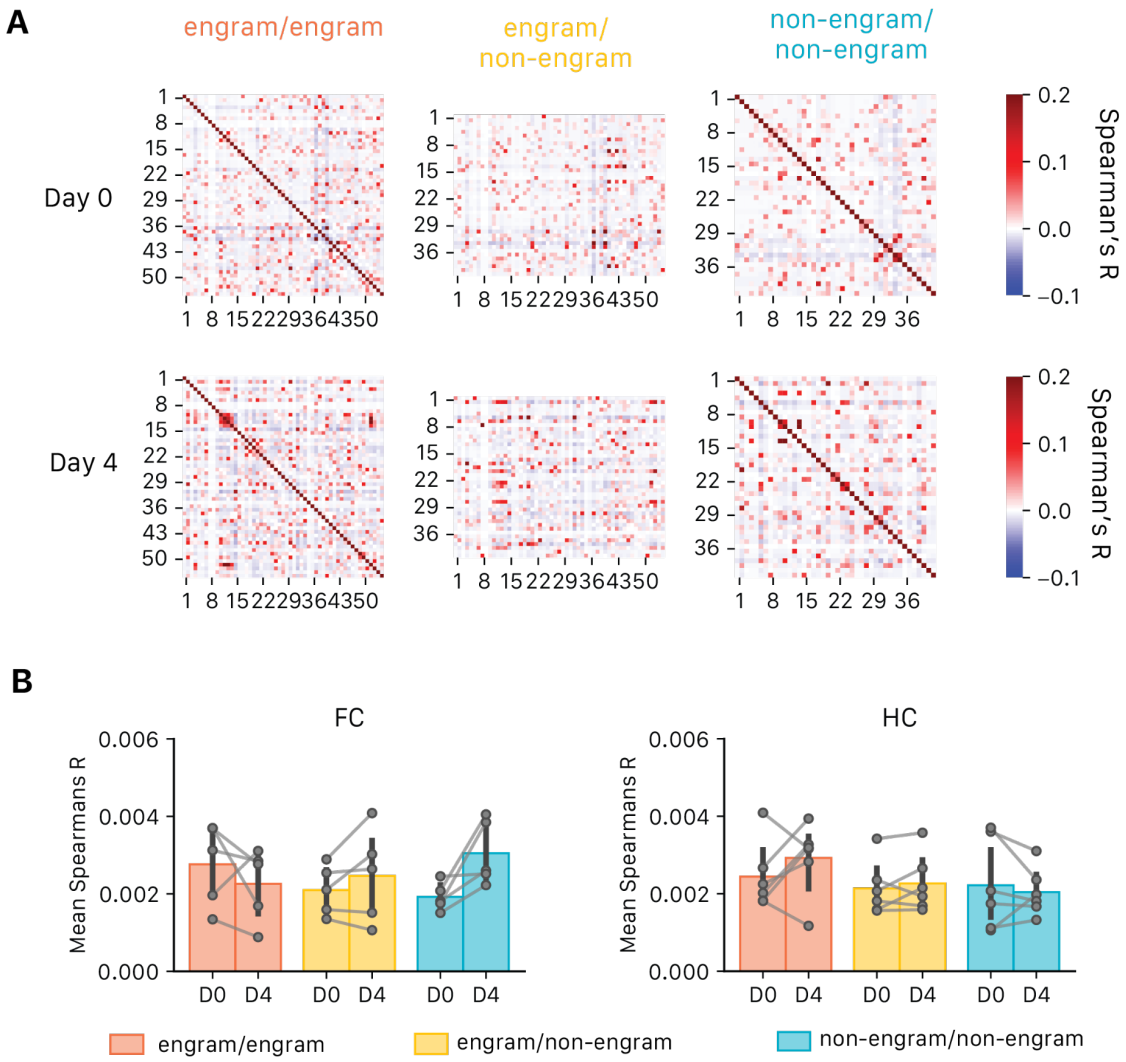

Figure 4. Mean correlations between engram cells do not increase

A) Example correlation matrices from cells on D0 and D4 in an example FC mouse. Left to right: engram/engram correlations, engram/non-engram correlations, non-engram/non-engram correlations. Cell ID sorting is consistent across both days.

B) Change in mean Spearman's correlation coefficient value from D0 to D4 for pairwise correlations between engram/engram cells (orange: E-E), engram/non-engram cells (yellow: E-N), and non-engram/non-engram cells (teal: N-N). One outlier HC mouse excluded. 2Way ANOVA Population x Day:
FC: Population F = 0.14, p = 0.87, Day F = 1.96 p = 0.19 Interaction p=0.05; Pairwise tests E-E p=1, E-N p=0.82, N-N p = 0.13,
HC: Population F = 0.93 p = 0.42, Day F = 0.65 p = 0.43, Interaction F=1.11, p=0.36; Pairwise tests E-E p= 0.90, E-N p=1.0 N-N p =1.0).

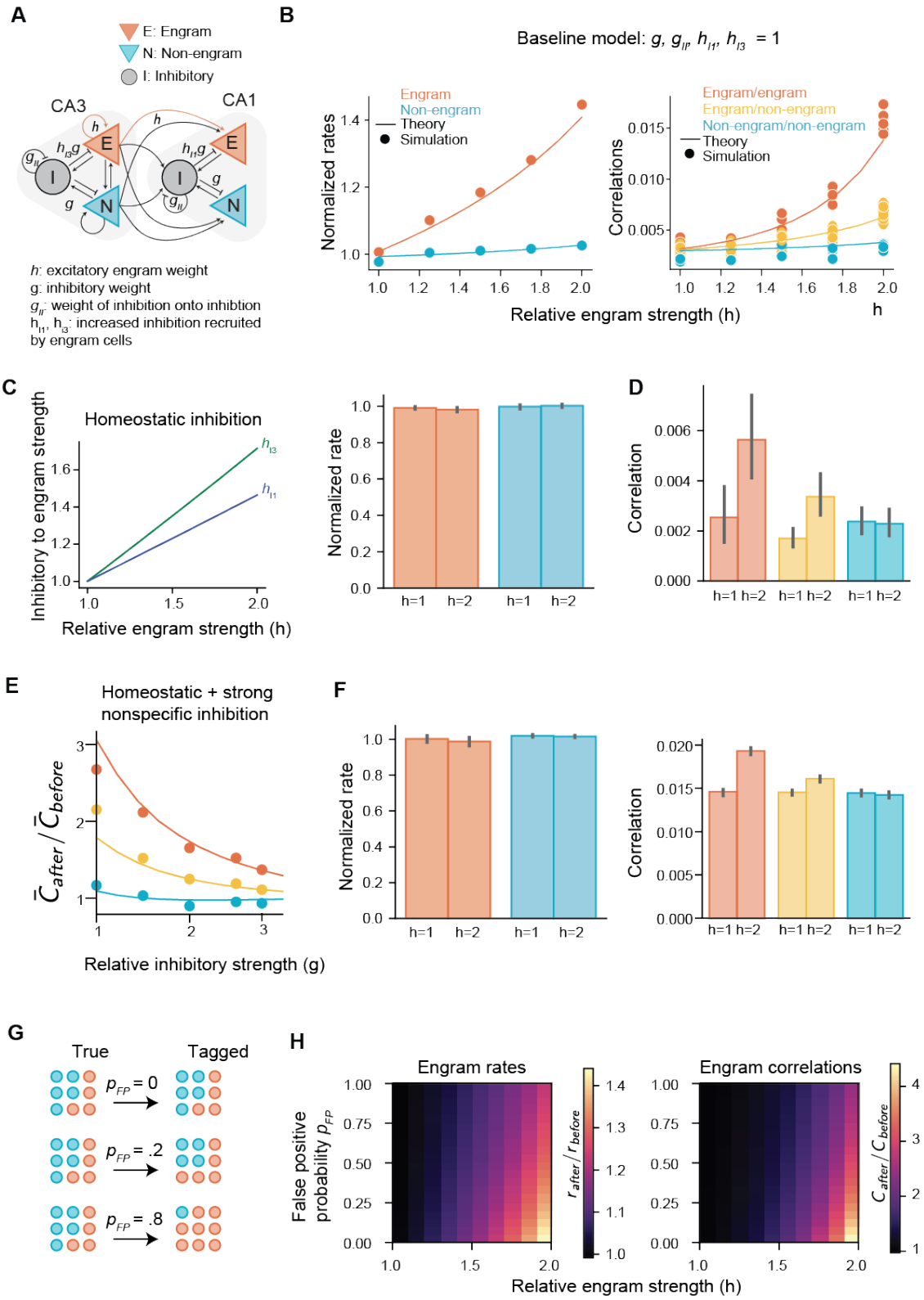

Figure 5. Spiking Model of CA3-CA1 Engram Dynamics

A) Schematic representation of model. A subset of cells are engram cells with excitatory weights specified by h. Inhibitory connections are specified by g, and inhibitory weights onto engram cells are scaled with h_{I3} *or* h_{I1} for CA3 and CA1 respectively.

B) In our baseline model, where inhibition and excitation have the same relative strength, rates (left) and correlations (right) of engram cells (orange lines) increase a large amount as a function of engram strength h.

C) (Left) The amount of homeostatic inhibitory plasticity, i.e. increased inhibition recruited by engram cells, needed to keep engram rates constant, as a function of the engram strength h. (Right) Simulated rates in both CA1 and CA3 before and after learning show that homeostatic inhibitory plasticity is able to keep both engram and non-engram rates constant.

D) Even with homeostatic inhibitory plasticity, pairwise correlations between engram cells increase with increased engram strength.

E) The ratio of correlations after potentiation of engram weights (h = 2) to before (h = 1) as a function of baseline inhibition g, incorporating the homeostatic inhibitory plasticity introduced in panel C. Stronger inhibition is able to decrease the change in correlation with increased engram strength.

F) (Left) Simulated rates in both CA1 and CA3 with strong inhibition keeps both engram and non-engram rates constant. (Right) Increased correlations between engram cells are suppressed in the high inhibition model.

G) Schematic for our noisy tagging. We assume all engram cells are correctly tagged, while non-engram cells are tagged with a false positive probability p_{FP}.

H) The ratio of engram rates (left) and engram-engram correlations (right) to their before learning (h=1) value as a function of engram strength h and false positive probability p_{FP}.

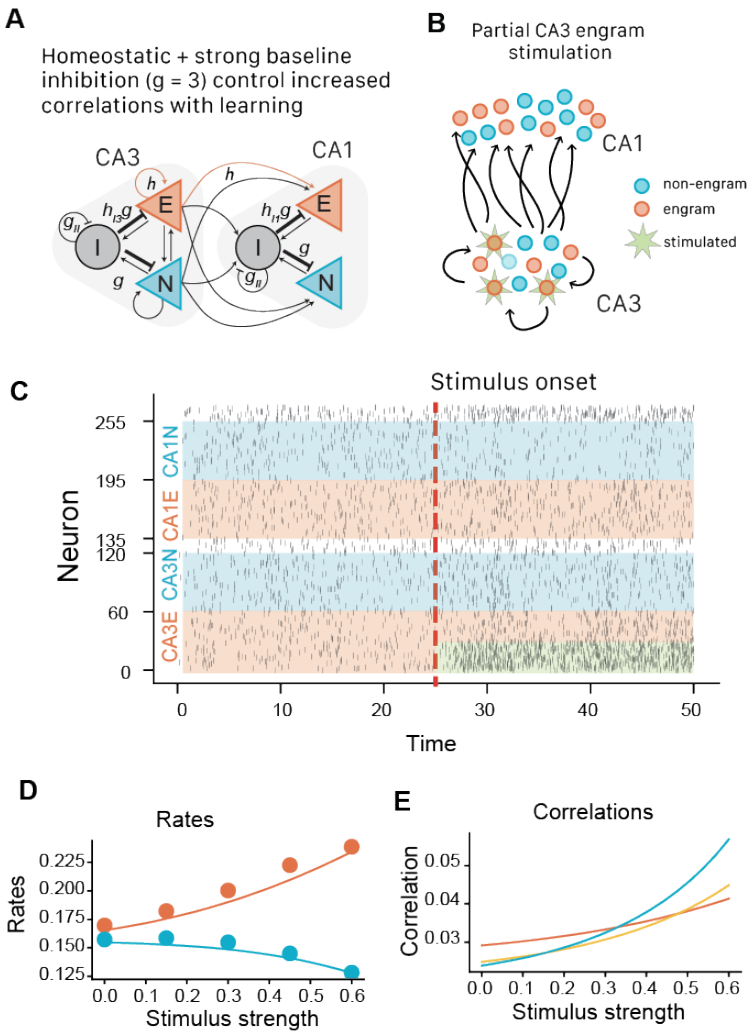

Figure 6. Engram Model Predictions

A) (Top) Summary schematic of updated network model including homeostatic inhibition (h_{I1}, h_{I3}, and higher inhibitory strength (g = 3). (Bottom) This model predicts a much smaller increase in engram-engram correlations following learning than our baseline model.

B) Cartoon of stimulation procedure and corresponding raster plot to test engram reactivation in the model. A subpopulation of CA3 engram cells received stimulation (time 25) reactivation.

C) Stimulating a portion of the CA3 engram cells leads to an increase in CA1 engram rates and a decrease in CA1 non-engram rates.

D) Stimulating a portion of the CA3 non-engram cells leads to an increase in pairwise correlation across all populations.

SUPPLEMENTARY FIGURES

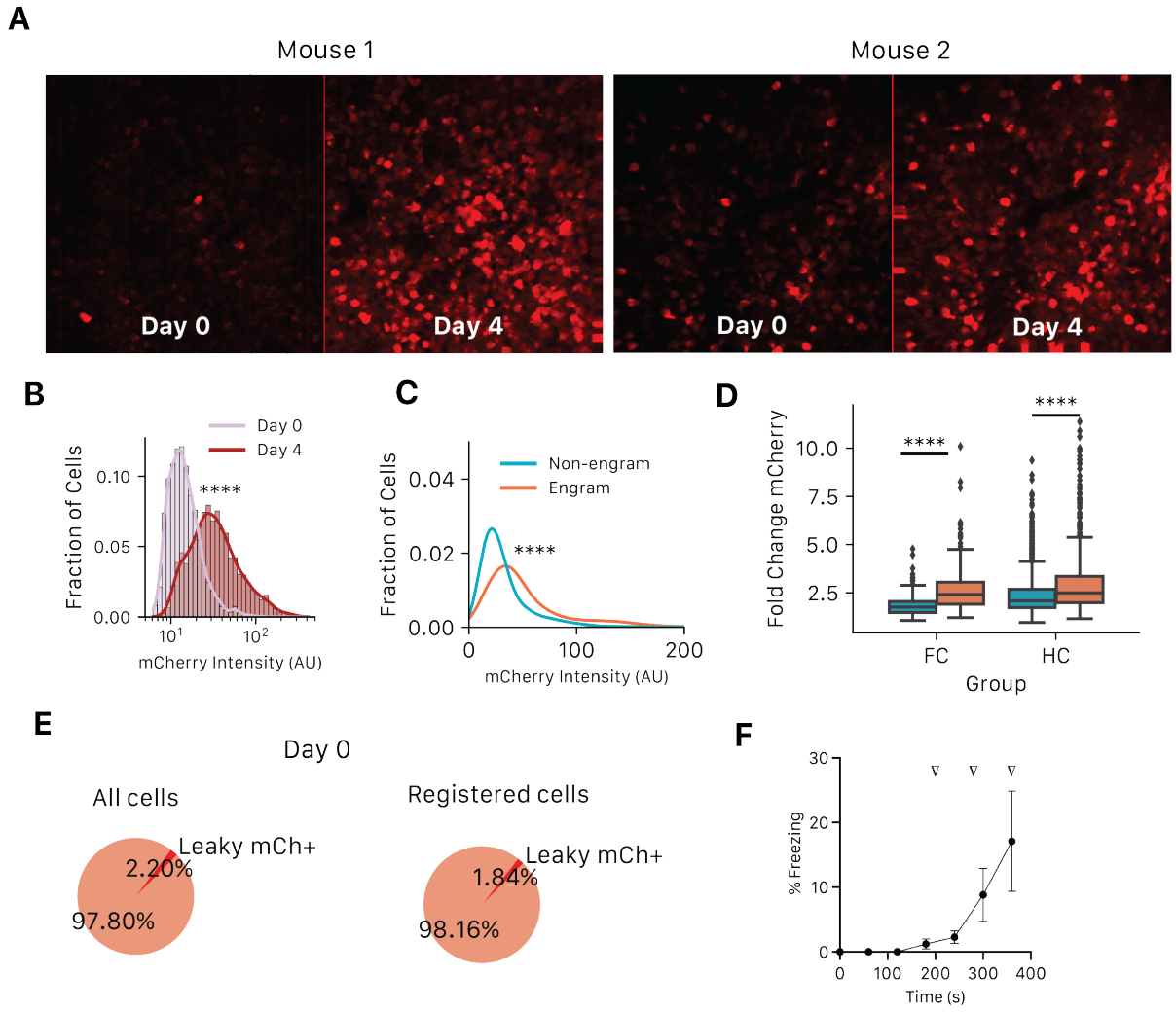

Supplementary Figure 1. TetTagging in vivo

A) Two example FOVs for tet-driven mCherry expression across days. mCherry tagging increases after Day 2 and is measured on Day 4.

B) Increase in mCherry intensity of cells quantified from Day 0 and Day 4. Wilcoxon signed-rank test W=119, p=0.0)

C) On Day 4, tagged engram cells had significantly higher expression of mCherry (Mann-Whitney U Test: U=674715, p<0.0001)

D) Engram cells in both FC and HC mice demonstrated a higher Fold Change in mCherry expression from Day 0 to Day 4 (FC Mann Whitney U Test U=39438, p<0.0001, HC U=118137, p<0.0001)

E) Percentage of active cells on Day 0 with high, leaky mCherry expression. Approximately 2% of active cells demonstrated high expression on Day 0 before tagging and were not classified as engram cells.
F) Percent time freezing during contextual fear conditioning. Arrows indicate shock times. Mice successfully increase freezing over the course of conditioning.

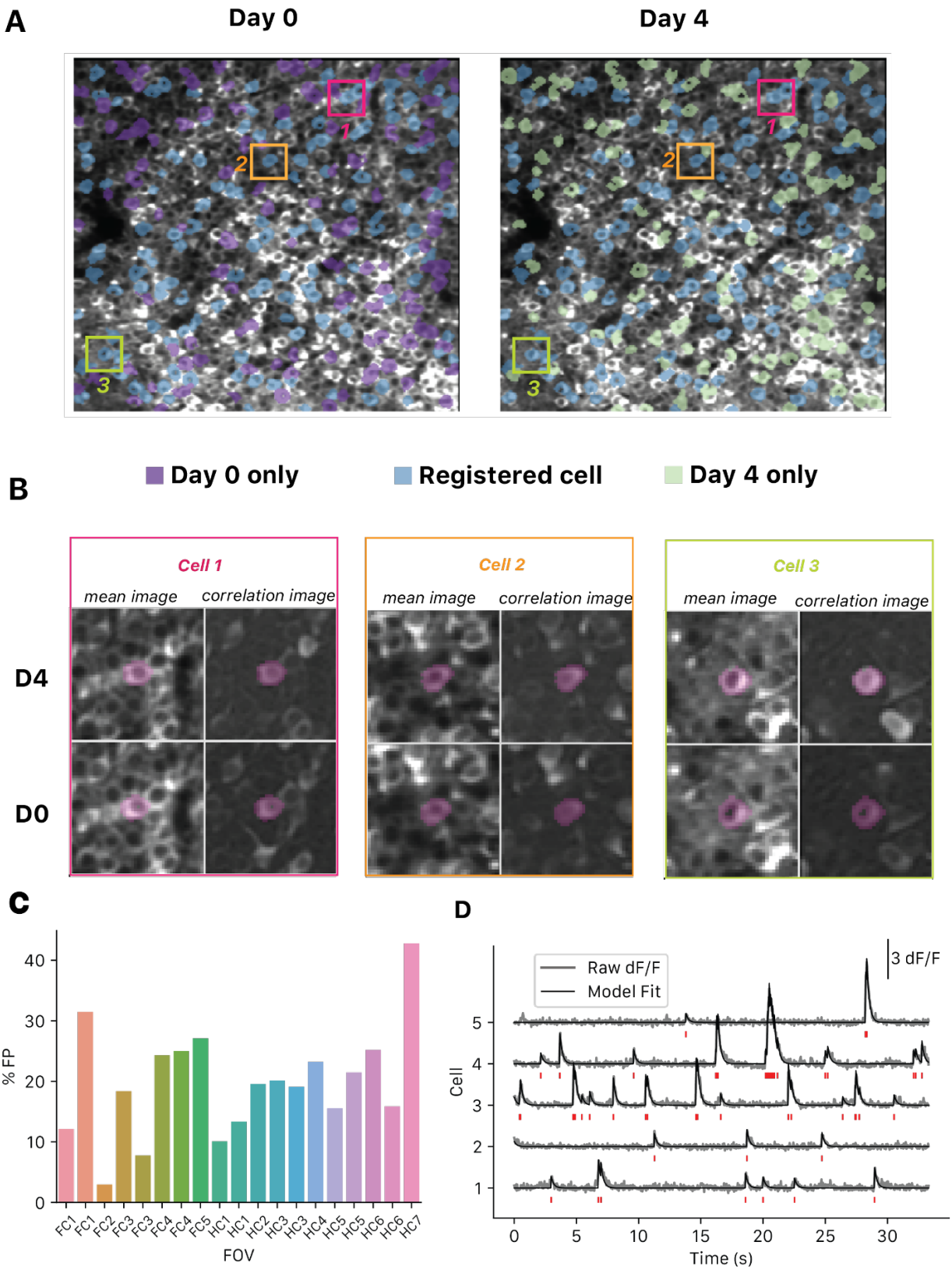

Supplementary Figure 2. Cell registration quantification and calcium deconvolution.

A) Example FOV of cell registration across 4 days. Blue cells: registered, green cells: D4 only, purple cells: D0 only
B) Example registered cell pairs plotted over mean projection image and correlation image on each day
C) Proportion of False Positive (FP) registered cell rois for each mouse/FOV. Manual evaluation of cells considered false positives if 1 of 3 criteria were met: 1) CNMF spatial footprint did not represent a true cell, 2) if the identified pair from CellReg was not a true match or 3) if CNMF spatial footprint overlapped between 2 cells. Across all FOVs, 19.8% +/- 2.1% of output rois from CNMF/CellReg were discarded.
D) Example dF/F traces with respective deconvolved events below. Deconvolution model fit (black) overlaid on top of raw dF/F (gray), calcium events shown below each transient (red).

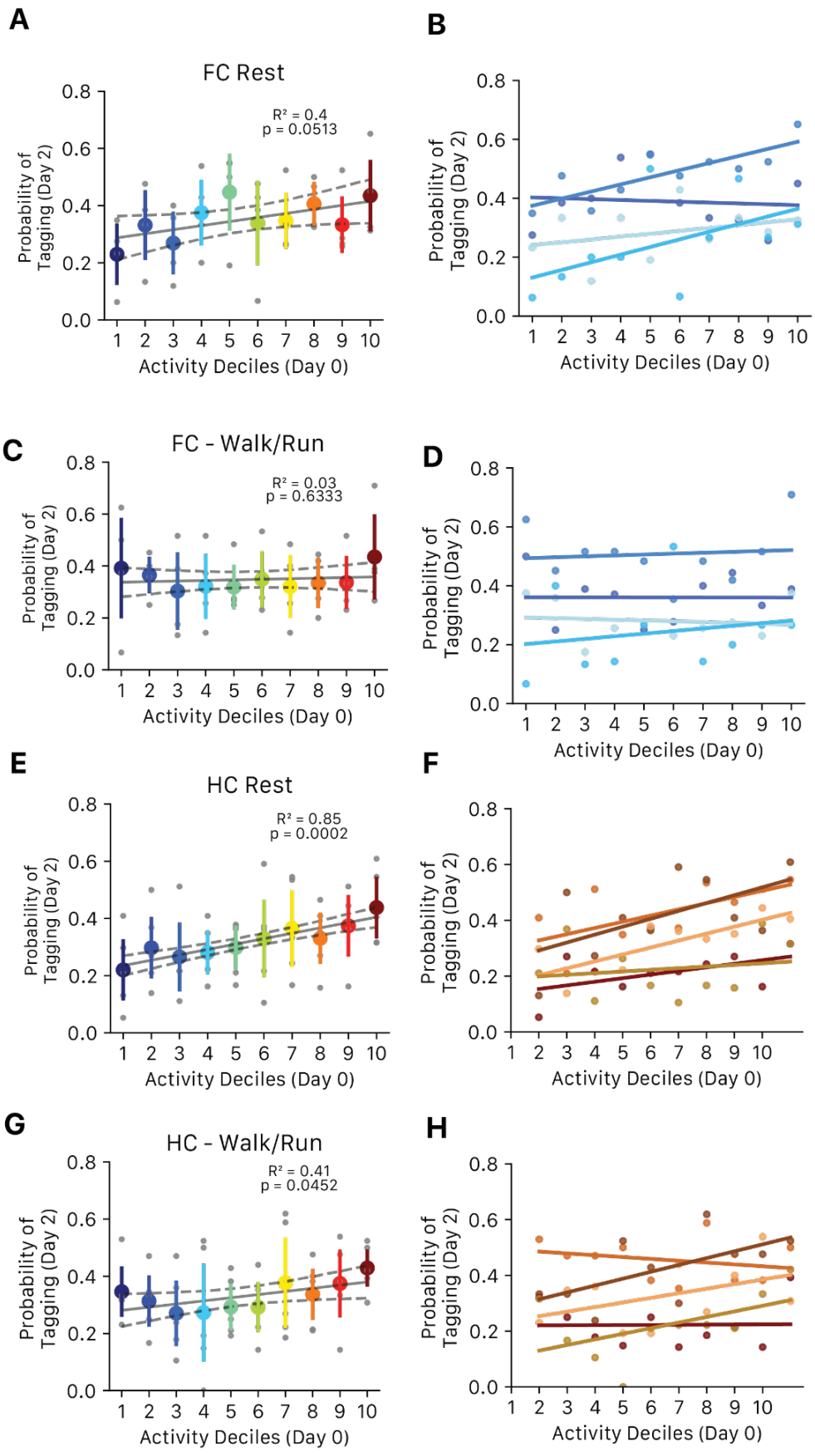

Supplementary Figure 3. Spontaneous activity during quiet rest better predicts allocation in FC and HC mice

A) Baseline (Day 0) activity correlates with probability of engram allocation during rest in FC mice (n=4). Linear Regression, R^2 = 0.4, p=0.0513
B) Individual trends for each FC mouse during rest (each colored line represents an individual mouse).
C) Baseline (Day 0) activity not correlated with probability of engram allocation during running in FC mice (n=4). Linear Regression, R^2 = 0.03, p=0.6333
D) Individual trends for each FC mouse during running (each colored line represents an individual mouse).
E) Baseline (Day 0) activity correlates with probability of engram allocation during rest in HC mice (n=5). Linear Regression, R^2 = 0.85, p=0.0002.
F) Individual trends for each HC mouse during rest (each colored line represents an individual mouse).
G) Baseline (Day 0) activity is only weakly correlated with probability of engram allocation during running in FC mice (n=4). Linear Regression, R^2 = 0.41, p=0.0452.
H) Individual trends for each HC mouse during run (each colored line represents an individual mouse).

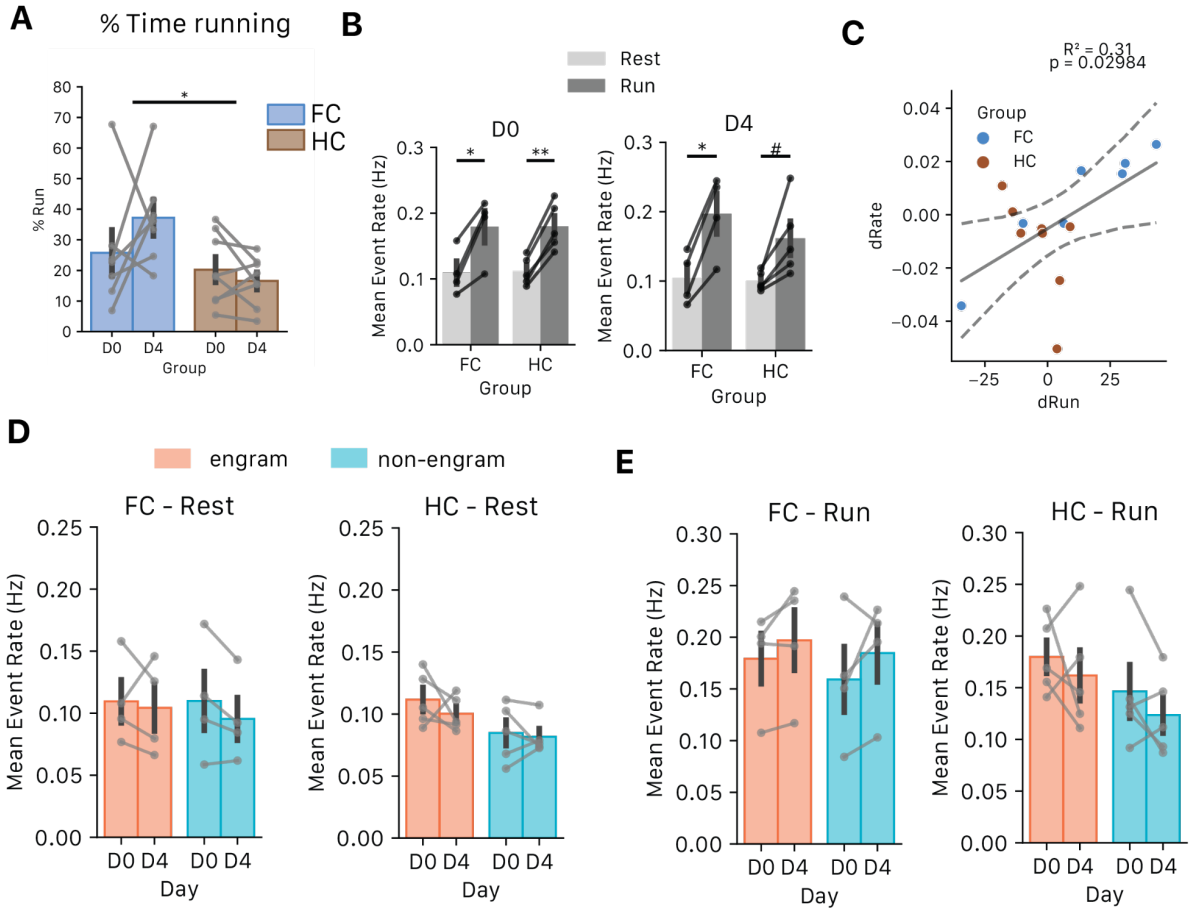

Supplementary Figure 4. Effect of locomotion on rates

A) % Time running for FC (blue) and HC (brown) groups; FC mice spent more time running. 2Way RM ANOVA Group x Session (Group: F=6.09 p=0.03 Session F=0.45, p=0.52, Interaction F=2.22 p=0.16; Pairwise tests FC D0 vs D4 p=0.61, HC D0 vs D4 p=0.64. Points represent FOVs from FC or HC animals.

B) Mean event rates during rest and run periods on each Day. Run periods had significantly higher event rates.

Left D0: 2Way RM ANOVA Group x State Group: F=0.0035 p=0.95, State F=73.3, p=0.0006, Interaction F=0.009, p=0.93. Pairwise tests (Rest vs Run) FC: p=0.043, HC p=0.0014. Points represent FOVs from FC or HC animals.

Right D4: 2Way RM ANOVA Group x State Group: F=0.55 p=0.48, State F = 34.1, p=0.0006, Interaction F=1.44, p=.27. Pairwise tests (Rest vs Run) FC: p=0.015, HC p=0.08.

C) Change in % time running correlates with change in mean event rate, suggesting running differences across sessions may affect overall observed activity. Linear regression, $R^2 = 0.31$, p=0.02984. Points represent FOVs from FC or HC animals.

D) No change in mean event rates on D0 vs D4 during rest periods only. 2Way RM ANOVA Population x Day.

FC: Population F=0.027, p=0.87, Day F=1.40, p=0.28, Interaction F=0.31, p=0.60. Pairwise tests (D0 vs D4) engram: p=1, non-engram p=0.26.

HC: Population F=5.99, p=0.04, Session F=0.97, p=0.35, Interaction F=0.32, p=0.59). Pairwise tests (D0 vs D4) engram: p=0.82, non-engram p=1. Points represent individual mice.

E) No change in mean event rates on D0 vs D4 during running periods only. 2Way RM ANOVA Population x Day.

FC: Population F=0.18 p=0.69, Day F=3.50, p=0.11, Interaction F=0.11, p=0.75. Pairwise tests (D0 vs D4) engram: p=0.34, non-engram p=0.62

HC: Population F=1.96, p=0.20, Session F=1.64, p=0.24, Interaction F=0.02, p=0.88). Pairwise tests (D0 vs D4) engram: p=1, non-engram p=0.51. Points represent individual mice.

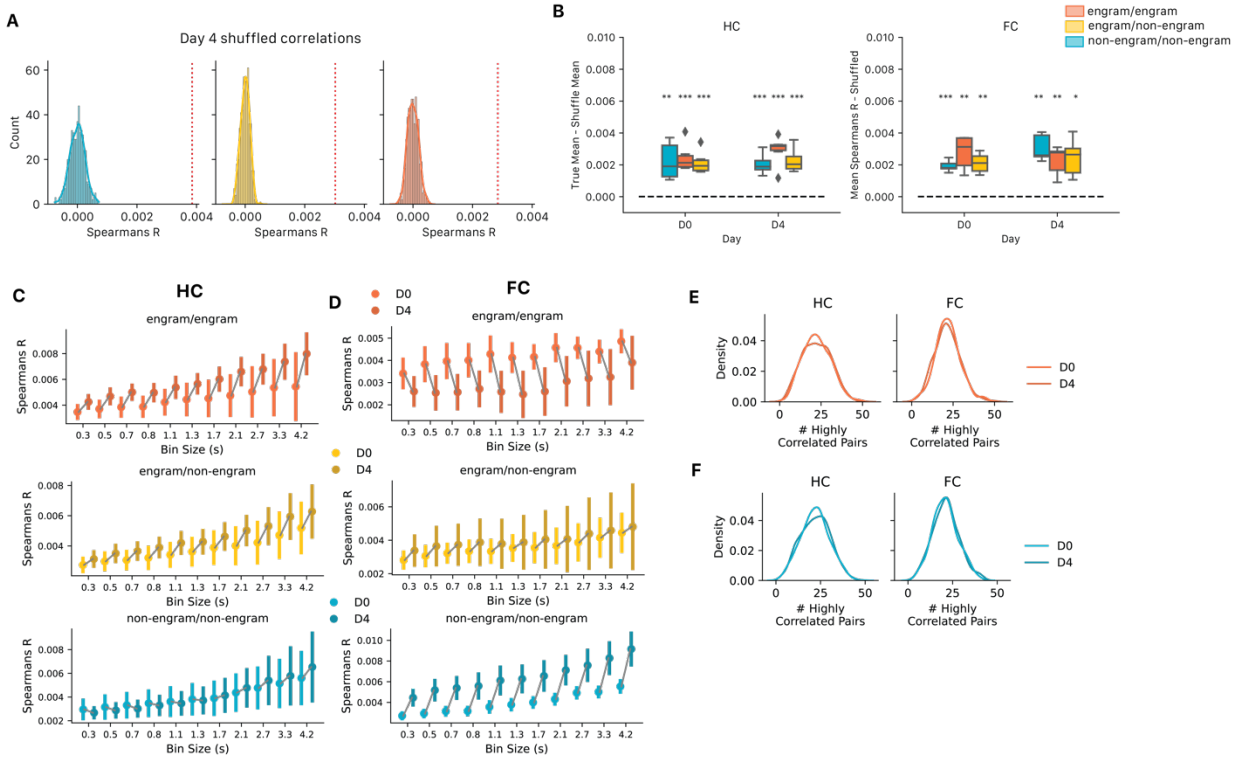

Supplementary Figure 5. Additional correlation analyses

A) Example distributions of mean shuffled correlations among populations for one session. True mean for each pairwise comparison shown in red dotted line for each panel

B) Difference in true mean Spearman coefficients and average of shuffle distribution for all mice. All groups are significantly different from zero (one-sample t-tests: * $p<0.05$, ** $p<0.01$, *** $p<0.001$)

C) Mean spearman correlations for binned traces from 0.3 s to 4.2 s bins in HC mice. Wilcoxon signed-rank test, D0 vs D4, all bins: engram/engram: $p=0.31$; engram/non-engram: $p=0.22$; non-engram/non-engram: $p=0.69$

D) Mean spearman correlations for binned traces from 0.3 s to 4.2 s bins in FC mice. Wilcoxon signed-rank test D0 vs D4, all bins: engram/engram: $p=0.19$, non-engram/non-engram: $p=0.13$. Paired t-test D0 vs D4, all bins: engram/non-engram: $p=0.64$

E) Distribution of # of highly correlated cells (upper 20% of all correlations) is unchanged from D0 to D4 in engram cells. (light orange: D0, dark orange: D4). Mann-Whitney test FC $p=0.58$, HC: $p=0.98$.

F) Distribution of # of highly correlated cells (upper 20% of all correlations) is unchanged from D0 to D4 in non-engram cells. (light teal: D0, dark orange: D4) Mann-Whitney test FC $p=0.59$, HC: $p=0.83$.

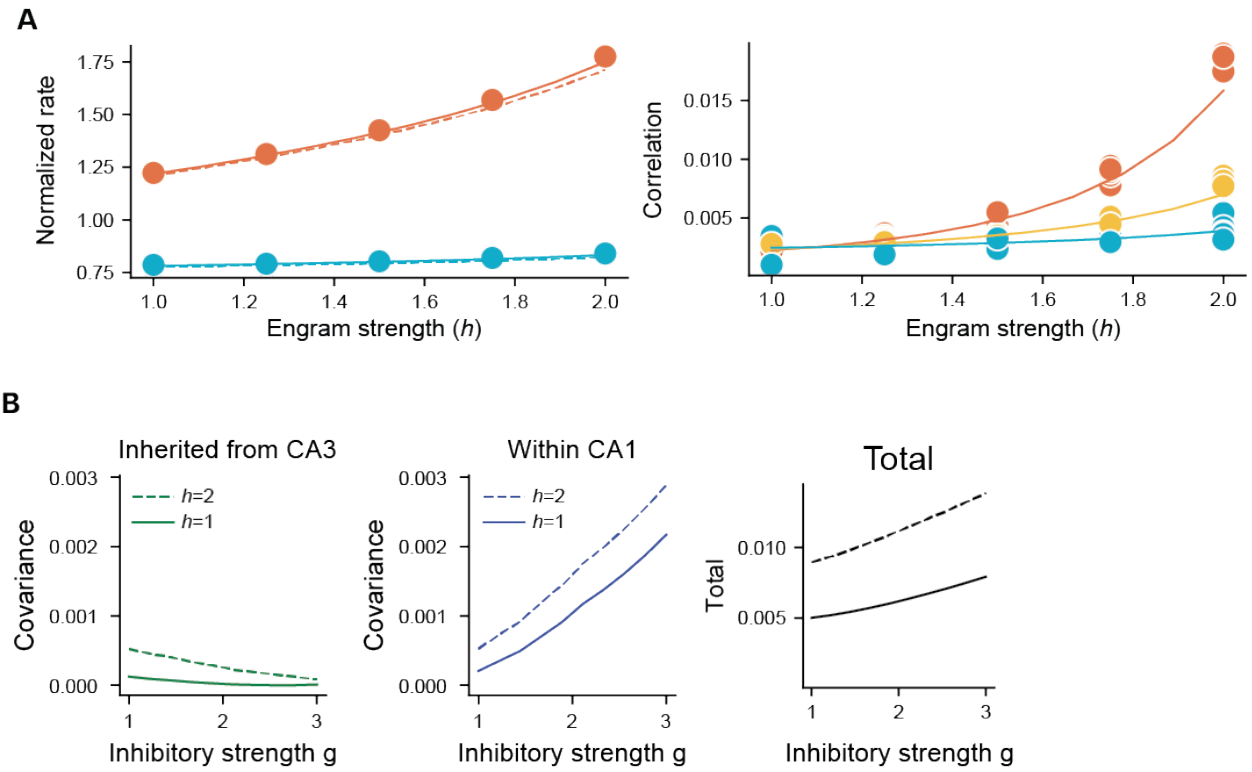

Supplementary Figure 6. Supplemental Model Analyses.

A) Model initialization with increased engram cell rates still displays an increase in rates (left) and correlations (right) between engram cells as *h* increases. Left: Engram cells (orange), Non-engram cells (teal). Right: engram/engram correlations (orange), Engram/Non-engram correlations (yellow) and non-engram/non-engram correlations (teal).

B) Because CA1 does not feedback to CA3, we can decompose the covariance in CA1 (right) into a part inherited from CA3 (left) and a part generated locally in CA1 via recurrent inhibition (center). Increased baseline inhibitory strength increases the share of correlations generated locally via recurrent inhibition (blue, within CA1), and reduces the change in correlation inherited from CA3 from before to after learning (green, CA3).